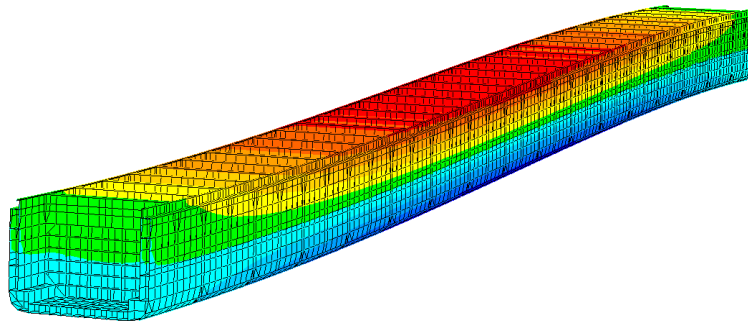


CHALMERS



Analysis of the effect of bending and torsion for fatigue in container ships

A comparison of current industry practices

Master's Thesis in the International Master's Programme Naval Architecture and Ocean Engineering

VIKTOR OGEMAN

Department of Shipping and Marine Technology
Division of Marine Design, Research Group Marine Structures
CHALMERS UNIVERSITY OF TECHNOLOGY
Göteborg, Sweden 2013
Master's Thesis X-13/291

MASTER'S THESIS IN THE INTERNATIONAL MASTER'S PROGRAMME IN
NAVAL ARCHITECTURE AND OCEAN ENGINEERING

Analysis of the effect of bending and torsion for fatigue in container ships

A comparison of current industry practices

VIKTOR OGEMAN

Department of Shipping and Marine Technology
Division of Marine Design
Research Group Marine Structures
CHALMERS UNIVERSITY OF TECHNOLOGY
Göteborg, Sweden 2013

Analysis of the effect of bending and torsion for fatigue in container ships –
A comparison of current industry practices
VIKTOR OGEMAN

© OGEMAN VIKTOR, 2013

Master's Thesis X-13/291
ISSN 1652-8557
Department of Shipping and Marine Technology
Division of Marine Design
Research Group Marine Structures
Chalmers University of Technology
SE-412 96 Göteborg
Sweden
Telephone: + 46 (0)31-772 1000

Cover:
Longitudinal stresses in ship-beam created by repetition of mid hold section under vertical bending.

Printed by Chalmers Reproservice
Göteborg, Sweden 2013

Analysis of the effect of bending and torsion for fatigue in container ships –
A comparison of current industry practices
*Master's Thesis in the International Master's Programme in Naval Architecture and
Ocean Engineering*
VIKTOR OGEMAN
Department of Shipping and Marine Technology
Division of Marine Design, Research Group Marine Structures
Chalmers University of Technology

ABSTRACT

Ocean-crossing vessels should be designed with sufficient fatigue strength. The high-cycle fatigue principle with specific S-N curves is used in the maritime industry to predict the fatigue life of ship structures. For conventional ship structures, the stress range distributions are provided by classification societies and are mainly based on empirical experience. However, a ship may change its designated trade region, leading to a change in encountered wave environment. This will create a discrepancy between design and actual stress range distribution. Furthermore, for a novel ship design, data of fatigue loads is not available to guide the structural design. Consequently, so-called direct calculation methods are introduced in order to compute the loads and corresponding structural stresses.

For the fatigue assessment of ship structures, the stresses are mainly caused by wave loads on the hull. These hydrodynamic loads can be computed using various theories and numerical implementations. As the method complexity increases, the computation may become more sensitive, leading to larger uncertainties. Moreover, usually, many different sea states with several operational conditions are considered, consuming much computational time in the early fatigue design stage.

The objective of this thesis is to study the efficiency and fatigue result of using different computational methods as well as the effect of fatigue damage contribution from bending and torsion. Different methods, from strip theory to advanced non-linear panel methods, are employed in order to estimate the hydrodynamic loads on a 4,400TEU container ship. Subsequently, the structural stresses are computed using both finite element methods and engineering beam theory combined with different options for local stress concentration. The corresponding fatigue damage is then estimated using various spectral methods and compared to direct rainflow counting to investigate the scatter.

Based on the results presented in this thesis it is concluded that a linear panel method for wave load analysis and engineering beam theory for structural stress calculation, combined with a simple spectral fatigue model, can give us accurate enough results and the most convenient/fast computation for simple details. However, at locations other than the mid-section, correct accounting for warping is required and an FE method is recommended.

Key words: Fatigue, Torsion, Spectral fatigue, FEM, Panel method, Rainflow counting, Strip theory, Direct calculation, Engineering beam theory

Analys av utmattningsbidragen från böjning och vridning i containerskepp –
En jämförelse av olika metoder

Examensarbete inom Naval Architecture and Ocean Engineering

VIKTOR OGEMAN

Institutionen för Sjöfart och Marin Teknik

Avdelningen för Marin Design, Forskargruppen Marine Structures

Chalmers Tekniska Högskola

SAMMANFATTNING

Fartyg bör designas med tillräcklig utmattningsstyrka. Vid utmattning genom många cykler används specifika S-N kurvor i den marina industrin för att förutspå livslängden för skeppsstrukturer. För konventionella designer ges fördelningen av spänningscykel amplituder av klassifikationssällskapens regler, mestadels baserat på empirisk erfarenhet. Men, ett skepp kan byta rutt och därigenom möta ett förändrat vågtillstånd. Detta skapar en skillnad mellan upplevd och designad spänningsdistribution och direkta metoder för att beräkna laster och de följande strukturella spänningar införs.

För utmattningsevaluering av skeppsstrukturer uppkommer de intressanta spänningarna på grund av våglaster på skrovet. Dessa laster kan beräknas genom olika teorier och numeriska implementeringar. När metodens komplexitet ökar så kan också känsligheten öka vilket leder till större osäkerheter. Dessutom utvärderas ofta många tillstånd, vilket kan göra processen tidskrävande.

Syftet med detta examensarbete är att undersöka effektiviteten och resultatet som fås från dessa olika numeriska metoder. Dessutom undersöks utmattningsbidraget från böjning och vridning av skrovet. Olika metoder, från strip-teori till avancerade icke-linjära panelmetoder, används för att uppskatta de hydrodynamiska lasterna på ett 4400TEU containerskepp. Därefter beräknas de strukturella spänningarna både genom finita elementmetoder och genom balkteori i kombination med olika val för stresskoncentration i detaljen. Den resulterande utmattningsskadan beräknas sedan med flera olika spektralmetoder och resultaten jämförs med det från regnflödesräkning.

Baserat på resultaten som presenteras så dras slutsatsen att linjära panelmetoder för våglastsanalys och balkteori för spänningsberäkningar i kombination med en enkel spektralmetod ger tillräckligt noggranna resultat och snabba beräkningar. Men, för detaljer på andra platser än i midsektionen krävs korrekt behandling av vridning och finita element metoder rekommenderas därför.

Nyckelord: Balkteori, Direkt beräkning, FEM, Panelmetod, Regnflödesräkning, Spektrala utmattningsmetoder, Strip-teori, Strukturella spänningar, Utmattning, Vridning

Contents

ABSTRACT	I
SAMMANFATTNING	II
CONTENTS	III
PREFACE	V
1 INTRODUCTION	1
1.1 Objectives	2
1.2 Methodology	2
1.3 Limitations	3
1.4 Outline of thesis	4
2 FATIGUE METHODOLOGY	5
2.1 Hydrodynamic loads	5
2.2 Girder stresses	7
2.3 Fatigue estimation	9
3 SHIP DETAILS AND BASIC SET-UP FOR THE CASE STUDY	11
3.1 The ship and detail	11
3.2 Sea environment	13
3.3 The ship FE model and software	14
3.4 Fatigue comparison reference	15
4 HYDRODYNAMIC ANALYSIS	17
4.1 Waves and sea states	17
4.2 Basic set-up in the computation	19
4.3 High frequency noise	24
4.4 Linear and non-linear panel methods	26
4.5 RAOs and strip theory	27
4.6 Concluding remarks	29
5 GLOBAL STRUCTURAL ANALYSIS	31
5.1 Cross sectional properties and forces	31
5.2 Beam theory and FE comparison	37

5.3	Component decomposition	39
5.4	The effect of horizontal bending and torsion	43
5.5	Concluding remarks	47
6	LOCAL STRUCTURAL STRESS ANALYSIS	49
6.1	Local stress evaluation methodology	49
6.2	SCF computation using different methods	51
6.3	Effects of SCF values due to local design	52
6.4	SCF computation using the global ship FE model	55
6.5	Concluding remarks	59
7	FATIGUE ASSESSMENT AND ANALYSIS	61
7.1	Concluding remarks	63
8	CONCLUSIONS AND PROPOSED METHODOLOGY	65
8.1	Proposed methodology	66
8.2	Further work	67
9	REFERENCES	68
	APPENDIX A – CROSS SECTIONAL PROPERTIES	71
	APPENDIX B – STABILITY IN HYDRODYNAMIC SOLVER	77

Preface

This thesis is a part of the requirements for a master's degree in Naval Architecture and Ocean Engineering from Chalmers University of Technology, Göteborg. It has been carried out at the Division of Marine Design, Department of Shipping and Marine Technology, Chalmers University of Technology between September 2012 and June of 2013.

First and foremost, I would like to thank my supervisor Assistant Professor Wengang Mao at the Department of Shipping and Marine Technology. Mr Mao has invested substantial time and commitment to helping me throughout the process of this thesis work and thereby taught me much. I would also like to acknowledge and thank my examiner, Professor Jonas Ringsberg, for his useful feedback and for organizing and accepting this Master's thesis project.

Additionally, I would like to mention PhD students Martin Kjellberg and Zhiyuan Li at the Department of Shipping and Marine Technology for contributing with knowledge and providing help on many occasions.

Göteborg, June, 2013

Viktor Ogeman

1 Introduction

Fatigue as used today, referring to the degradation of material due to repeated cyclic loading was first introduced in the 1840s and 50s in connection with the railway industry. Public awareness of the issue of fatigue was raised as a consequence of the famous Versailles railway accident of 1842 which cost 40 to 80 people their lives. The accident was caused by the failure of one of the axles due to fatigue, Smith (1990).

The expression fatigue does, however, have a longer history: it was used already in the days of long sea voyages to less formally refer to the strain of the masts of the ships due to the repeated hoisting of sails, Suresh (1991). Although much of the historical development in the field has been connected to railway and aircraft applications, fatigue has also had a profound effect on the maritime industry. Probably the most famous example of fatigue accidents in ships is the brittle fractures in the mass-produced Liberty ships during World War II. Initially, the new welding processes used were suspected as the cause of the numerous accidents, but later investigations showed that the low temperatures on the North Atlantic lead to brittle fatigue failures in the untested steel alloys. These failures lead to a substantial effort being put into investigations of pre-existing cracks and stress concentrations around discontinuities, Smith (1990).

These and other accidents clearly show the importance of considering fatigue strength when designing ships. It is also acknowledged by the classification societies, and today all major classification societies have requirements on ships' fatigue strength. In shipping the high-cycle fatigue method is most often used for analysing the fatigue life of a structural detail. This method typically combines the Palmgren-Miner law with S-N curves that describe the fatigue life of the material under cyclic loads, DNV (2010a).

In the ship fatigue assessment, problems such as material properties, defects, residual stresses, surface finishing, etc., create a large variation in fatigue life even under similar circumstances. This is commonly accounted for by safety margins in the S-N curves, DNV (2010a). The large uncertainties in ship fatigue life design can be illustrated by the difference found by applying guidelines from different classification societies. For example, different guidelines have been shown to produce a predicted fatigue life between 1.8 and 20.7 years in a pad detail on the longitudinal coaming of a particular Panamax container ship, Fricke et al. (2002). The differences are mainly explained by the choice of S-N curves and local stress computations. However, the different wave environments provided by these classification societies also contribute significantly to the variation in fatigue life predictions.

Furthermore, container ships are particularly subjected to many fatigue problems. Usually, stresses due to vertical bending contribute to the major part of accumulated fatigue damage in ship structures. However, the often long and slender hulls of container ships combined with the open cross section mean that both horizontal bending and torsion effects are more pronounced than for other ship types, Mao (2010). These large differences and previously described uncertainties motivate this study. It is of particular interest to investigate what choices of methods or parameters have the greatest impact on the predicted fatigue damage and how a consistent and accurate fatigue damage prediction may be obtained. An additional factor is the

computational intensity of several direct calculation methods used today. Accurate fatigue prediction should ideally be achievable in reasonable time in order to allow for easy assessment during conceptual design stages to avoid later design problems.

1.1 Objectives

The main objective of this thesis is to improve current industry practices for fatigue damage calculation by suggesting a simple and reliable direct fatigue assessment procedure with acceptable accuracy for ship structural details. This may be broken into several sub-objectives such as:

- Describe the phenomena of fatigue failure in engineering structures.
- Investigate the advantages and disadvantages of different fatigue assessment methodologies.
- Propose a more accurate method for computing cross sectional forces and moments using pressure distributions from panel method solvers.
- Demonstrate that engineering beam theory can be used to accurately predict fatigue damage if the correct cross sectional loads are given.
- Show the relative importance of the longitudinal stress created by vertical bending moment, horizontal bending moment and torsion to a ship's fatigue assessment.
- Demonstrate that frequency domain fatigue estimation is sufficiently accurate to replace the direct rainflow counting method for uniaxial stress.

The motivation for studying these issues is primarily the trend to use more and more advanced and time-consuming methods for fatigue evaluation, at times with little apparent gain with respect to accuracy. It is believed that, especially for simple geometries, substantial time gains may be achieved without increasing errors in the fatigue life prediction.

Shipping is today regarded both as a good transportation option from a sustainability perspective, and as a large-scale example of pollution due to using, for example, low grade fuels. Therefore, ensuring that shipping continues to be a competitive and yet sustainable alternative for commodity transportation in the future will become an increasingly more important area. By constructing a more precise damage prediction model material over-usage may be limited, but, more importantly, the fatigue life of ship hulls may be improved, thus reducing the net life cycle effect of the ship.

1.2 Methodology

Fatigue assessment in marine structures may be split into four parts, illustrated in Figure 1. The methods in each part can be interchanged to allow for many different calculation procedures. To evaluate the fatigue damage of a structural detail using the methodology outlined in Figure 1, the first step is to compute the hydrodynamic loads acting on the ship, DNV (2010a). These can be computed using a linear frequency

domain analysis, for example strip theory, or using more advanced time domain simulations such as panel methods or viscous CFD methods.

The structural stresses caused by these wave loads are then sought for. Engineering beam theory or a global FE model of the girder may be combined with either a tabulated stress concentration factor (SCF) or a detailed FE analysis in order to account for the concentration of stresses due to the local geometry.

Finally, the fatigue damage is computed using either the rainflow counting method or a spectral method, based on an appropriate S-N curve, DNV (2010a).

This thesis tries to find a path through Figure 1 that combines the ease of use with reliable and sufficiently accurate results. This is done by choosing a standard combination of methods and individually exchanging one of the steps, investigating the result on the computed fatigue accumulation.

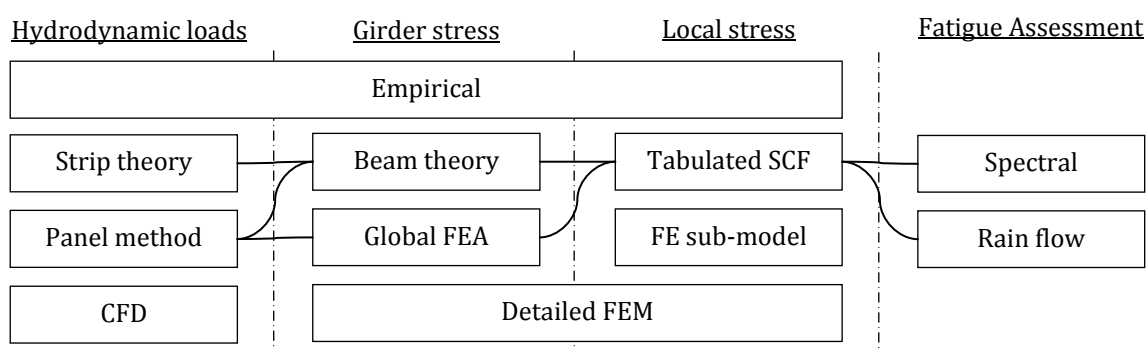


Figure 1. An overview of methods and different steps used for calculating fatigue damage in ship structures using the high-cycle fatigue principle.

1.3 Limitations

There are several large international classification societies dictating fatigue requirements for all their larger ships. Due to limited time only the rules, procedures and software produced by DNV (Det Norske Veritas) have been investigated. It is assumed that these provide a representative view of how fatigue assessment is performed in industry today. Furthermore, only one particular ship has been used throughout this work. This 4400 TEU container ship (see Section 3 for more details) was chosen because of the availability of a global FE model.

Also, only the global structural forces have been considered in the current fatigue assessment. Effects such as local tank or water pressures, sloshing, etc., have not been considered. The analysis is additionally limited to uniaxial stress. Finally, only a few, and in particular one, structural detail has been considered. This is due to lack of time, and the considered detail is therefore assumed to be representative for details in the mid-ship region under global uniaxial load. This will limit the generality of any conclusions drawn from this thesis. However, the ship is geometrically representative of this class of ships. Further the location considered is in the most critical area, where fatigue strength in general should be checked.

In addition, only a stress-based fatigues analysis is performed, ignoring residual stresses or effects from the environment, such as corrosion. All structural analyses have been performed using a quasi-static FE analysis.

Among these, the assumptions of no residual stresses and corrosion are thought to be the most problematic. However, complete coverage of all cases is beyond the scope of this thesis. It is hoped that these simplifying assumptions will provide a good indication for the results under additional effects and it is likely that per-case investigation will in any event be needed at later design stages.

1.4 Outline of thesis

This thesis has been split into four main parts corresponding to the steps introduced in Figure 1 for ship fatigue assessment. First, a brief overview of the fatigue assessment framework is given in Section 2. Subsequently, Section 3 introduces the investigated ship and the considered structural detail used as the case study for the comparison of different fatigue assessment methods.

This is followed by the investigation and comparison of different options for the computation of hydrodynamic loads in Section 4, the options for global structural stress calculation in Section 5 and the resulting local stresses and effects in Section 6. Section 7 compares different methodologies for evaluating the accumulated fatigue damage in the structure detail. Each of these chapters presents both the findings and some discussion on those results.

Finally, Section 8 presents the general conclusions and the proposed fatigue assessment procedure based on the previously presented findings.

2 Fatigue methodology

This section introduces part of the theory underlying the different steps in the fatigue assessment procedure. These steps were briefly introduced in the previous section. This introduction is not meant to be a complete reference for the competent reader, but is rather to be viewed as a brief introduction only discussing the parts relevant for the purpose of this thesis. As such, it focuses on the methodologies commonly used in the maritime industry.

Referring back to Figure 1 a selection of the different methods available for assessing fatigue damage is presented. Here, the process is largely divided into four stages: the evaluation of hydrodynamic loads, the calculation of girder stresses, the corresponding local structure effects and resulting stress in the considered detail. Finally, the fatigue damage caused by the stresses is estimated.

Now, in parallel to the four stages described in Figure 1, the fatigue assessment procedure of a ship detail may be split into two different main methodologies: a time domain analysis or a spectral fatigue evaluation, Mao (2010).

Time domain analysis is based on the calculation of the stress history in a particular detail, or the stress from measurements. Fatigue damage caused by these stresses (calculated or measured) is then computed by the so-called rainflow counting method. In spectral fatigue evaluation, the exact stress history in the detail is not needed. Instead, the stress spectrums are used directly in order to approximate the fatigue damage.

2.1 Hydrodynamic loads

In this thesis, two methods for evaluation of hydrodynamic loads are used: strip theory and panel method solvers. These methods use different approximations to compute the motions of the ship for a given set of waves. The forces acting on the ship hull can be also computed simultaneously. More details of these two methods will be described in the following sub-sections. Additionally, some brief comments on sea states, wave spreading and response amplitude operators are introduced.

2.1.1 Strip theory

Linear strip theory is based on the assumption that 3D effects due to hull geometry change, for example the flow around bow and stern, and ship motions are small. This implies that the ship being considered is slender, the ship speed is moderate and the sea waves are small relative to the size of the ship. Using these assumptions the coefficients for restoring force, damping and added mass of the ship may be evaluated by summation of the properties of 2D strips of the ship, Janson (2012).

For ship fatigue assessment, strip theory is commonly used for computing the wave loads. This is because of its low computational requirements and robustness, experience show that it works well even when the assumptions are violated. Recently, the effects on the result due to the underlying assumptions, for example linearity, have been questioned, Li and Ringsberg (2011).

2.1.2 Panel methods

Panel methods mediate some of the issues with strip theory. They are based on 3D solutions to potential flow theory in the time domain. This combined with appropriate boundary conditions allow for solutions in arbitrary non-viscous wave descriptions and the inclusion of some forward speed effects, DNV (2011c).

Effectively a differential equation of a damped motion in six degrees of freedom is solved for the ship, given by

$$M\ddot{x}(t) + B\dot{x}(t) + Cx(t) = F(t) . \quad (1)$$

Here $x(t)$ is the ship's motion over time, M is the total mass (including added mass) and B , C are coefficients describing the damping and restoring forces on the ship respectively. Given the time-varying external loads $F(t)$, and solving this differential equation gives the ship motions over time. This external force is a function of the ship's position and the water surface height surrounding the ship. In the current hydrodynamic analysis, a Rankine panel method is used for solving the Bernoulli equation with free surface boundary conditions, DNV (2011c).

In a linear panel method only the terms introduced in Eq. (1) are used. The external forces are computed using the mean water surface to remove non-linearity in the hydrodynamic force. However, various additional non-linear terms may be included in order to obtain a more realistic model. The non-linear properties considered in the non-linear panel solver in this thesis are: (DNV (2011c))

- Integration of Froude-Krylov forces (the force by undisturbed waves of the ship hull) on the instantaneous wetted surface instead of the mean wetted surface.
- Quadratic terms in the Bernoulli equation are included.
- Exact rotations in inertia and gravity terms.
- Inclusion of a quadratic roll damping term.

A real ship is kept on course using an active rudder. It is used to compensate for forces trying to change the ship's course. Instead of a rudder, the current panel solver uses a spring control system introducing restoring forces to keep the surge, sway and yaw centered around zero, DNV (2011c).

2.1.3 Response amplitude operators and sea states

In linear theory, waves are described as a sum of harmonics of different frequencies, where the phases are often taken to be uniformly distributed. This means that the spectrum, i.e. the amount of energy content at different frequencies, is enough to generate a wave surface for a sea, Ditlevsen (2002).

There exist several standard formulae to describe these spectra, using different parameters to match empirical wave data from different circumstances. In this thesis, the two-parameter Pierson-Moscowitz spectrum is used, described by (Janson, 2012)

$$S_{PM}(\omega) = \frac{1.25}{4} H_s^2 \frac{\omega_m^4}{\omega^5} e^{-1.25 \left(\frac{\omega_m}{\omega} \right)^4}. \quad (2)$$

Here, ω is the angular frequency, H_s is the significant wave height and ω_m is the modal frequency which can be related to the mean peak period of the waves. Generally, a sea state is comprised of not only waves from one direction, but is a superposition of wave systems from many angles. To account for this, a spreading function D is introduced, which, instead, describes the sea state as a weighted sum of waves from all directions. In this thesis, the spreading factor is described by

$$D(\varphi) = \begin{cases} \frac{2}{\pi} \cos^2(\varphi) & |\varphi| < \frac{\pi}{2} \\ 0 & \text{otherwise} \end{cases}, \quad (3)$$

where φ is the angle between the considered components and the main sea direction, Janson (2012). Now, a ship operating in a sea state will normally move with a steady forward velocity thereby changing the apparent wave system encountered. A ship in deep seas operated with a forward velocity U and a heading angle θ from a wave with the frequency ω will experience an encountering frequency of

$$\omega_e = \omega - \frac{\omega^2 U}{g} \cos(\theta), \quad (4)$$

where g is the acceleration due to gravity, Lewis (1989).

When considering the ship-sea interaction as a linear system, response amplitude operators (RAOs) are often used to describe the ship's response under various harmonic wave components. A RAO is the ratio between the magnitude of the response, for example the horizontal bending or heave motion, and the amplitude of the harmonic wave. In a linear system a harmonic exciting force (wave) will create a response of the same frequency, albeit possibly with a phase offset. These RAOs are represented by functions describing this ratio as a function of the encountering wave frequency. Note that different heading angles and different ship speeds lead to different curves, Janson (2012).

The advantage of these response amplitude operators is that by constructing them for all heading angles, ship speeds and encountering wave frequencies of interest the linear ship motion in any sea state can easily later be computed by a summation of the frequency components. Note that care must be taken to account for the phase lag when combining different responses.

2.2 Girder stresses

Given the forces acting on the ship hull, a method is needed to compute the stresses in the hull girder caused by these forces. The two methods used for this in this thesis are briefly introduced below.

However, first a short qualitative discussion on the stresses present in the ship hull when subjected to external forces. The global deformation of the ship girder may be

divided into four main components: axial compression, vertical bending, horizontal bending and torsion, or twist, of the ship hull. Figure 2 illustrates the longitudinal stress distribution in the cross section under the last three of these deformation modes.

Under axial compression or tension of the hull longitudinal stresses can be regarded as being evenly distributed through all longitudinally continuous fibres. During vertical bending due to hogging the upper part of the hull will be in tension and the lower parts in compression as illustrated to the left in Figure 2. The stress distribution during horizontal bending is similar, Li (2011).

Due to the presence of bulkheads the longitudinal displacement, warping, of the cross section during torsion is prevented, leading to longitudinal stresses as illustrated to the right in Figure 2. Note that both vertical and horizontal bending stresses are expected to obtain their maximal values (in the absolute sense) in the outer deck region. Also, the warping stresses are expected to be close to their largest values here.

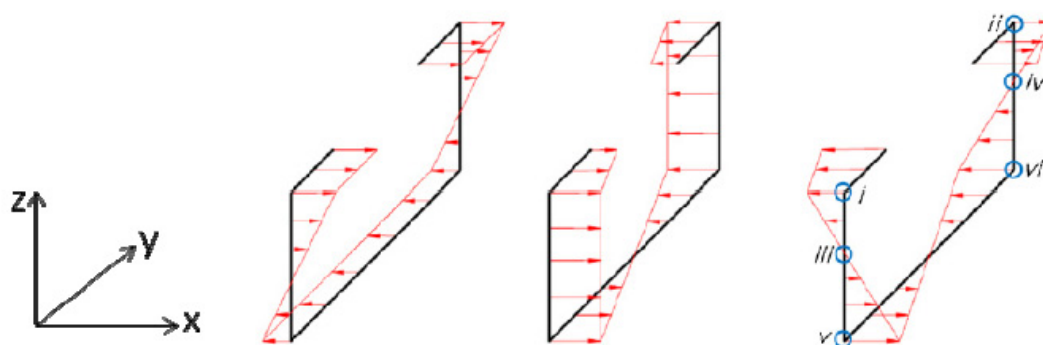


Figure 2. Longitudinal stress distribution in the cross section under vertical bending, horizontal bending and torsion, respectively, Li (2011).

2.2.1 Engineering beam theory

Given all forces acting on the ship hull the resulting forces and moments needed for keeping any two parts of the ship together may readily be found using statics. Thereby the bending moments, shear forces and axial forces through any cross section of the ship can be found.

Now, engineering beam theory allows for calculation of stresses in any location in the cross section of a beam. Based on the assumptions of small displacements, unchanged sectional geometry, an initial straight and prismatic beam and linear elasticity the stress in any position of any cross section is given by

$$\sigma_l = \frac{F_n}{A} + \frac{M_v}{I_v} \Delta z + \frac{M_h}{I_h} \Delta y + \sigma_w, \quad (5)$$

where F_n, M_v, M_h are the longitudinal force, and the vertical and horizontal bending moment, respectively. The properties A, I_v, I_h define the cross-sectional area and area moments of inertia, while $\Delta z, \Delta y$ are the distances between the detail and the neutral axes, and σ_w is the stress due to warping, Thelandersson (1987).

Thus, by regarding the ship as a prismatic beam with the cross sectional geometry of the section of interest, an approximation of the longitudinal stress in any detail in this section may be found using Eq. (5). Despite its severe assumptions, engineering beam theory has been shown to be applicable in many situations, including when these assumptions are violated such as when the cross-section is only partly prismatic, DNV (2010a).

2.2.2 FE analysis

Alternatively, the girder stresses may be calculated using a global FE model of the ship. The ship is then typically discretized and described by a model consisting of beam and shell elements. Instead of transferring sectional loads from the hydrodynamic calculation, the calculated hydrodynamic water pressures can directly be transferred as pressures on the corresponding elements. This also allows for a locally more detailed analysis of the load effects. The stress in the detail of interest can then be evaluated by interpolating stresses obtained in elements in the ship FE model.

Having obtained the solution of the global hull girder model, a sub-modelling technique can be used to obtain a more detailed stress distribution in the detail. During this process the displacements calculated for the global model are transferred as boundary conditions to the edges of more refined models. This enables investigation of the stresses in local geometry, DNV (2011e). An outline of this process repeated four time is illustrated in Figure 3.

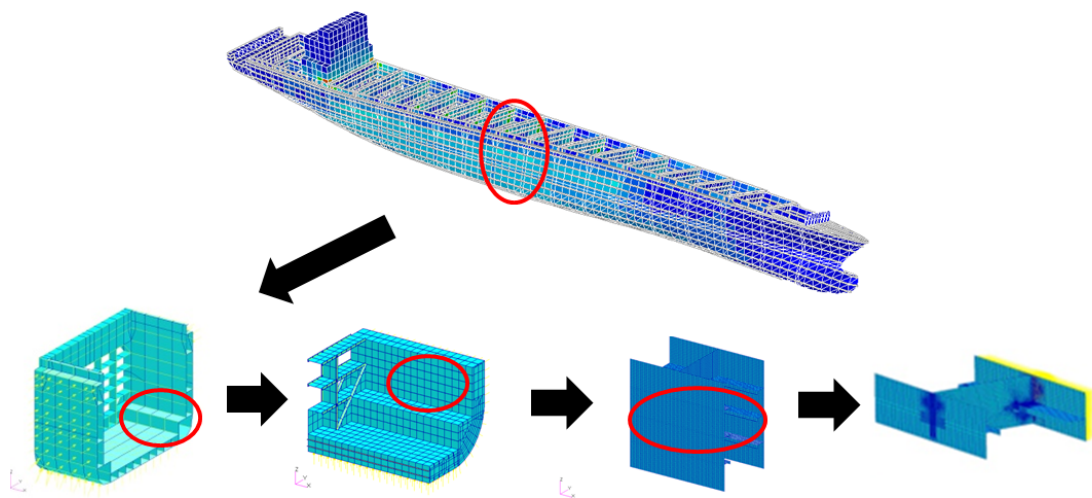


Figure 3. Illustration of a multi-stage sub-modelling technique, Li (2011).

2.3 Fatigue estimation

High-cycle fatigue estimation is based on linear elastic stress response and S-N curves describing material strength against fatigue failure. In this approach, the number of load cycles occurring at different cycle amplitudes should be obtained. The damage from each amplitude level is often determined from experimental data (the S-N curves). The damages from the different levels are combined in order to calculate the total corresponding fatigue damage. Often, the linear Palmgren-Miner rule is used for accumulating the total damage, given by

$$D = \sum \frac{n_i}{N_i}, \quad (6)$$

where n_i is the number of cycles at a particular amplitude level and N_i is the number of cycles until failure for that stress level. D is the total damage and material failure is often taken as $D > 1$. When the stress history of a structural detail is available, the rainflow counting method is commonly used for extracting the stress cycles, Rychlik (1993). A one-slope log-linear S-N curve, with parameters α, m , may, for example, be described as

$$\log(N) = \alpha - m \log(S), \quad (7)$$

Alternatively, the fatigue damage can be estimated using a spectral fatigue method given the spectrum of the structural stresses. The so-called narrow band approximation is often used for ship fatigue assessment. Given a stationary Gaussian load, the narrow band approximation (NBA) is an upper bound to the rainflow damage. It tends to the same value for narrow band processes, Rychlik (1993). The NBA may be calculated according to (α, m as above)

$$D^{\text{NB}} = \frac{T(2\sqrt{2})^m}{2\pi\alpha} \sqrt{\lambda_2} \lambda_0^{(m-1)/2} \Gamma(1 + m/2), \quad (8)$$

where T is the considered period, λ_i is the i^{th} spectral moment and Γ is the gamma function.

There exist several corrections to the NBA for wider, two-peak load spectrums or even for non-Gaussian processes, see, for example, Mao, (2010), Benasciutti and Tovo, (2007). Such methods use spectral properties, often moments, or work by splitting the spectrum into parts, to approximate the damage.

3 Ship details and basic set-up for the case study

Most of this thesis is based on a case study of a particular ship, using a particular set of rules as described in the section on limitations. This section aims at introducing this case study in more detail. An image of the considered ship during operations may be seen in Figure 4.

First, the ship is introduced along with some main particular and motivation for the choice of this particular ship. The location and some properties of the stiffener bracket detail used for most of the analysis is also described. Subsequently, the numerical FE model of the ship is detailed followed by the operating environment and the choices made with regard to that. The software used for performing all calculations in this thesis is also described. Finally, the default set-up used for calculating fatigue damage in the detail is described. Since fatigue damage comparisons are used throughout the thesis, these settings are needed to ensure consistent comparisons when changing one or another of the available methods.



Figure 4. Image of the considered container ship with 4,400TEU capacity.

3.1 The ship and detail

The ship is a 294-metre long, 4400 TEU, container ship built in 2003, normally operating in the North Atlantic. The ship is built to DNV class Container Carrier and the main particulars for the vessel are found in Table 1. Although the listed service speed is 23 knots the ship speed has been assumed to be 10 m/s (about 19.5 knots) for all calculations in this thesis.

This ship was chosen because it has a conventional cross sectional design and is of a common size. It is therefore considered to be representative of container ships, and, through this, increases the likelihood of measures constructed on this ship being correct for other vessels also. Additionally, this particular ship was chosen due to the availability of stress sensor data from full size measurements during operations on the North Atlantic. Finally, an FE model of the hull girder was available to the author.

Table 1. *Main particulars of the vessel, Storhaug & Moe (2007).*

Length overall	294.0 m
Length between perpendiculars	281.0 m
Breadth	32.26 m
Depth	21.50 m
Design draught	10.78 m
Deadweight	47754 tonnes
Service speed	23.0 knots
Block coefficient	0.69

The ship is a conventional container ship with a long mid-section of unchanged geometry, see Figure 5. Similarly to other container ships it has an open cross-section and the ship is longitudinally divided into holds by bulkheads. The shear strake and upper deck of this ship is made of 60mm plates and the hatch coaming of 65mm plating. Two different measures of the cross-sectional properties are available and presented in Table 2. The first set of measures is obtained by direct integration of the structural members from the ship drawings, without any correction applied for effects such as effective flanges or corrosion margins. The second set of properties is obtained from estimations in DNV Nauticus, Storhaug & Moe (2007).

Table 2. *Sectional properties of the mid-section. The values from NAUTICUS estimation are taken from Storhaug and Moe, Storhaug & Moe (2007).*

	Direct calculation	NAUTICUS
Neutral axis above baseline	10.05 m	10.31 m
Vertical area moment of inertia	334.6 m ⁴	351.8 m ⁴
Horizontal area moment of inertia	782.4 m ⁴	796.2 m ⁴
Cross sectional area	4.57 m ²	4.61 m ²

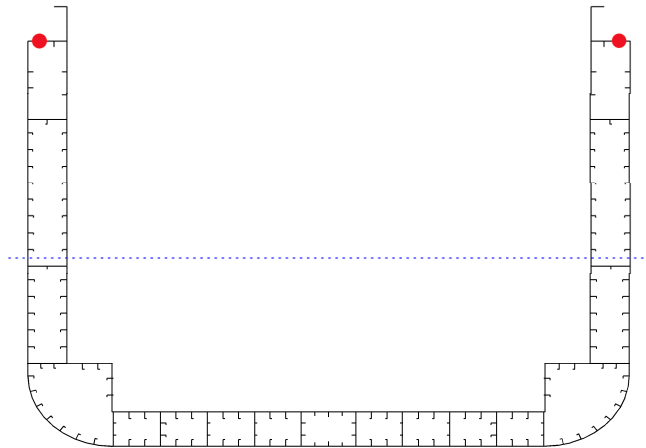


Figure 5. *Transversal section amidships with the neutral axis marked as a dotted blue line and the two locations of interest marked with red dots.*

The structural detail considered in all calculations except one is the weld toe at the end of a bracket as connected to the outermost deck longitudinal in the middle of the middle hold (about 133.5 m forward of the aft perpendicular). The detail's location in the cross section may be seen in Figure 5 and an illustration of the geometry surrounding the detail in Figure 6. The detail is located 21.65 m above the base line and 15.5 m from the ship's centre line.

This detail is chosen because of the uniaxial load as well as the absence of local pressures such as from tanks or sea. This detail is further located at a position where longitudinal stresses due to both vertical and horizontal bending moments are expected to attain almost maximal values. Similarly, the detail is located at a position in the cross section where torsion is expected to be significant, although longitudinally as far distant as possible from any bulkheads restricting warping.

An illustration of the detail with the weld at which root the hot-spot considered is located is shown in Figure 6. More details are presented in Section 6.

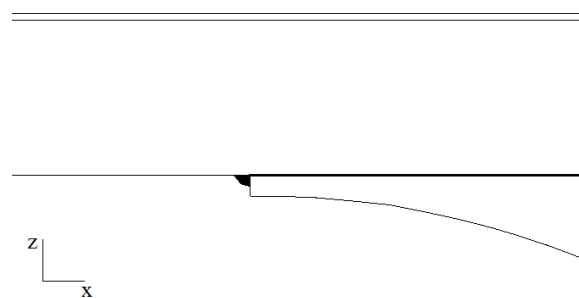


Figure 6. *A local view of the detail as seen from the side of the ship. At the top, the deck plating is illustrated with the stiffener below. At bottom the weld and the bracket is seen.*

3.2 Sea environment

When computing wave loads, a stationary sea state is often described by the Pierson-Moskowitz (PM) spectra with the two parameters, the peak period T_p and significant

wave height H_s . In the current study, only the most probable peak wave period is chosen for a given significant wave height. All the investigated sea states are listed in Table 3, where T_p is chosen based on the wave scatter diagram in DNV Fatigue Note 30.7, DNV (2010a). Unless otherwise specified, the sea states are further described as short crested sea with a spreading factor of $\cos^2(\phi)$, no swell is considered.

Table 3. *The most probable peak periods on the North Atlantic for given significant wave heights (DNV, 2010a).*

H_s	T_p	H_s	T_p	H_s	T_p
0.5 m	9.15 s	3.5 m	12 s	6.5 m	14.8 s
1.5 m	10.6 s	4.5 m	13.4 s	7.5 m	14.8 s
2.5 m	12 s	5.5 m	13.4 s	8.5 m	14.8 s

3.3 The ship FE model and software

The ship FE model consists of shell and beam elements, in accordance with the DNV guidelines found in classification notes 31.7 (DNV, 2011e). To obtain a non-singular solution the FE model is constrained for translation in the after perpendicular (AP) and bow hull underside. Additionally, to prevent rotation about the lengthwise axis, a node in the aft deck was constrained for translation in the breadthwise direction, see Figure 7 for a diagram of the model and boundary conditions.

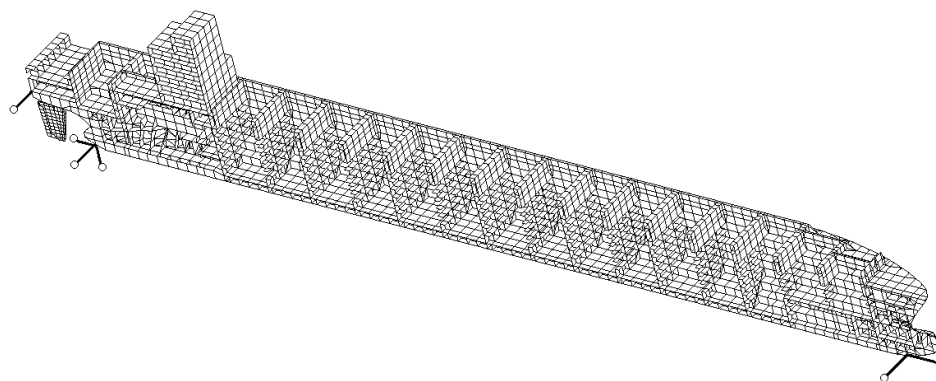


Figure 7. *A view of a half-ship FE model with marked boundary conditions. Note that while the model is symmetric all calculations have been performed on a complete ship model, since the wave loads and accelerations are not symmetric.*

The software package DNV Sesam, DNV (2011b) has been used for all hydrodynamic and structural computations. In particular HydroD v4.5-08 has been used for configuration of hydrodynamical simulations. For strip theory calculations Waveship 6.2-05 has been used, while Wasim v5.1-0.3 was used for time domain panel method simulations. For frequency domain calculations Postresp v6.3-0.1 and in-house scripts have been used.

For structural calculations Sesam explorer v4.0-03 has been used combined with Sestra64 v8.4-04 as a finite element solver. For modelling of FE geometries Patran Sesam 2010.2.3 was used. To transfer displacements between global FE solutions and models of local geometries Submod v3.2-02 was used and for extraction of stresses from FE models, Xtract v3.0-00.

For post-processing and data analysis Matlab with the Wafo toolbox, Brodtkorb, et al. (2000) has been used.

3.4 Fatigue comparison reference

To allow for easy evaluation of the effect of changing methods to perform one of the steps described in Figure 1 a reference fatigue assessment procedure is introduced. This section will briefly specify how such a calculation is performed. To understand why these specific methods were chosen, the following sections are to be referred to.

The hydrodynamic loads are calculated using a linear panel method solver, using the settings described in Section 4. To calculate the resulting global stress, beam theory is used with terms for only vertical and horizontal bending moment, calculated as (see also Section 5)

$$\sigma_l = \frac{M_v}{335} 11.55 \pm \frac{M_h}{655} 15.5 \quad (9)$$

for the starboard and port side, respectively. This global stress is then transferred to a local stress in the detail using the arbitrary stress concentration factor 2.0. This choice is unimportant since all comparisons are normalized against the reference fatigue values.

Finally, the fatigue accumulation is calculated using the Palmgren-Miner law combined with a one-slope S-N curve described by (DNV (2010a))

$$\log_{10}(N) = 12.164 - 3.0 \log_{10}(S). \quad (10)$$

The stress cycles are extracted from the rainflow counting method.

4 Hydrodynamic analysis

This section introduces the procedures used for calculating the hydrodynamic loads on the ship. The girder stresses change due to different predicted hydrodynamic loads, resulting in different fatigue damages predictions. To mitigate these differences a consistent set-up is introduced for the panel solver. Additionally, the difference in fatigue accumulation using different settings is investigated.

First, the effect of using different wave descriptions and methods for generating sea states is investigated. This is coupled with an investigation into the required simulation time to obtain a steady damage rate. Therefore, the stationary period of the sea state can be found.

This is followed by an investigation on the convergence of the panel method solver. Several problems are encountered and described. A set-up used for solving for the ship motion using the panel method solver, both linear and non-linear, is described. Additionally, a method for removing unwanted noise from the output signals is described.

Finally, a damage prediction comparison is made. The damage calculated using frequency domain damage computations with strip theory and panel methods is compared to the damage from time domain calculations.

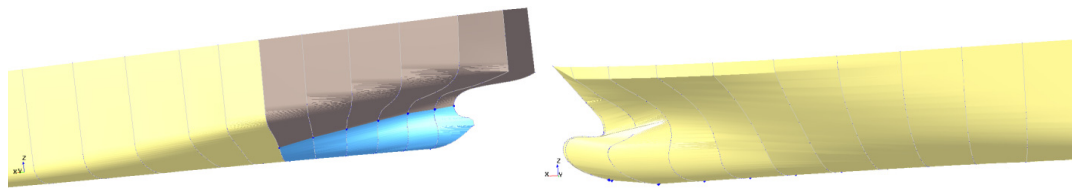


Figure 8. *A hydrodynamic model of a ship as modelled in the software. The three patches used for generating a mesh for the ship is shaded in different colours.*

4.1 Waves and sea states

To quantify the difference in fatigue damage from using different wave descriptions, an investigation of the ship in regular bow waves is made. Table 4 shows the difference in computed stress- cycle range and fatigue damage when the ship is subjected to harmonic waves and Stoke's fifth-order waves, Ditlevsen (2002). The waves are of the same height. The corresponding stresses are calculated using an engineering beam theory. The non-linear solver is used in both cases.

As expected, the difference is larger for steeper waves, reaching a difference of up to 11% in 8 m waves. However, such high waves are exceedingly rare under ordinary circumstances. For smaller waves the difference is within a few per cent and is therefore not considered. All further simulations are made using harmonic waves. The difference between the two sides might be explained by the π rad phase difference in σ_h interfering constructive and destructive, respectively, with σ_v .

Table 4. Under-prediction of fatigue damage and stress amplitude using harmonic wave description as compared to fifth- order Stoke's description with a non-linear solver in 200 m long regular bow waves. The numbers refer to under-prediction for the corresponding measure. Specifically, longitudinal stress in detail due to vertical, horizontal, horizontal and vertical bending as well as fatigue damage calculated using rainflow counting is shown.

H_s (m)	Side	$\Delta\sigma_v^*$	$\Delta\sigma_h^*$	$\Delta\sigma_{h+v}^*$	d^*
8	Starboard	1.7%	-3.7%	3.8%	11%
8	Port	1.7%	-3.7%	0.56%	1.7%
4	Starboard	0.68%	0.0%	2.5%	5.1%
4	Port	0.68%	0.0%	0.44%	0.3%
2	Starboard	0.14%	0.37%	0.43%	1.4%
2	Port	0.14%	0.37%	0.0%	0.0%

In the hydrodynamic analysis, the waves are generated based on linear wave theory. Two different algorithms were used to generate wave surface for sea states, randomly subdividing the spectrum into a finite number of frequency components and uniform spreading of the wave frequencies. Note that with the default option in the hydrodynamic solver of random subdivision, the generated wave surfaces are not Gaussian distributed as expected, see Table 5 and Figure 9. Here, the distribution of surface height using the two methods is compared to the theoretically expected normal distribution.

All subsequent simulations in this investigation use the uniform option with 500 components and a spreading factor of $\cos^2(\phi)$.

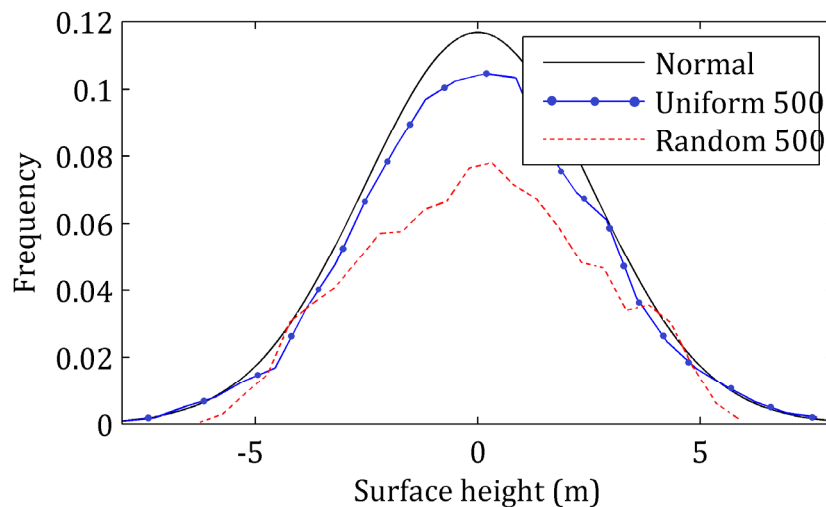


Figure 9. Histograms of wave surface elevation using two generating methods and a reference normal distribution.

Table 5 Excess kurtosis γ_2 of wave surface for various sea states described by a PM spectrum and generated by a random subdivision of 500 wave components. For a normal distribution $\gamma_2 = 0$ is expected. Increasing the number of components does not significantly change the values.

H_s (m)	Method	$E[\gamma_2]$	$\sqrt{\text{Var}[\gamma_2]}$
2.5	Random subdivision	-0.678	0.022
2.5	Uniform subdivision	-0.072	0.173
4.5	Random subdivision	-0.691	0.023
4.5	Uniform subdivision	0.079	0.162

To ensure that all sea state simulations were sufficiently long to obtain steady damage rate estimations, the convergence for three combinations of settings were studied. Some of the results are presented in Figure 10.

It is concluded that for reasonably small wave heights, 1,800s is sufficient for obtaining a steady damage rate. This simulation length is subsequently used. For a significant wave height of 5.5 m, which is still relatively common in the North Atlantic, DNV (2010a), the coefficient of variation in damage rate was less than 7%, which is considered acceptable.

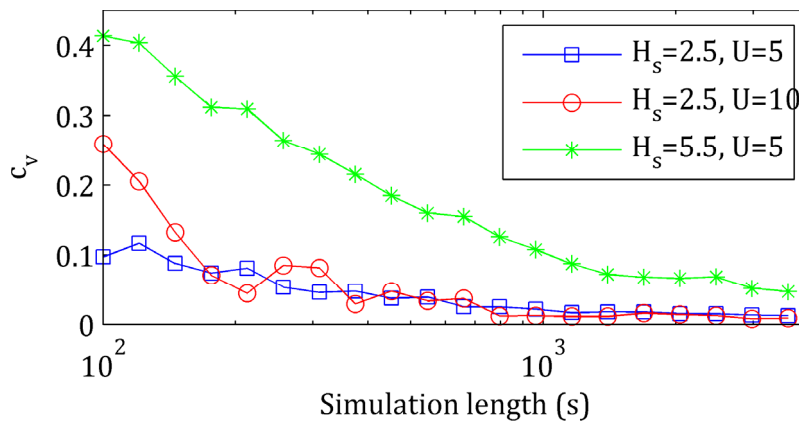


Figure 10. Coefficient of variation in a predicted damage rate from 200 realizations using the rainflow counting method and engineering beam theory to combine the vertical and horizontal bending moment. A linear panel method solver is used for both cases with a speed of 5 m/s, and non-linear for 10 m/s. Note the logarithmic abscissa scale.

4.2 Basic set-up in the computation

This section will introduce some of the tests carried out for obtaining a working set-up for the hydrodynamic analysis. In particular, the settings for the panel method solver

in Wasim are investigated. Additional investigations and motivations can be found in Appendix B.

First, the dependence on the panel mesh is investigated, followed by an investigation into the stability of the solver when using different ship stabilising spring system settings.

These tests lead to the conclusion that in order to find the hydrodynamic loads a 2,800 seconds (s) long linear panel method simulation is to be performed in Wasim. A sea state for a given H_s is generated according to Section 4.1, above, and the ship model is discretized by 42x12, 12x12 and 12x8 elements for patches one, two and three, respectively. The ship draught is set to 10.98 m corresponding to a fully laden condition and the sectional forces are extracted as calculated by Wasim for the location of the detail (133.5, 0, 10.3). The stabilising spring system is configured to have periods of 60 s, 30s and 30 s, respectively and a damping coefficient of 0.1 for all three directions. The simulation is performed with a time step of 0.05 s and a ramp length of 240 s. The simulation is allowed to stabilize for 1,000 s before fatigue data is extracted.

4.2.1 Hydrodynamic panel mesh

To investigate the sensitivity of the simulation to the mesh size, two additional meshes in addition to the default suggested on import of the hull geometry into the solver were tried. The ship hull is meshed by the three patches as in Figure 8. The mesh density for these can be found in Table 6.

Table 6. *A summary of settings for the three different panel meshes on the hull.*

Patch	Default Settings	Mesh 2	Mesh 3
Patch 1	35x5	42x12	60x16
Patch 2	5x5	12x12	16x16
Patch 3	8x5	12x8	16x10

The effect of different mesh sizes to the computation is investigated using a harmonic sea state with an incident angle of 135 degrees. It is found that there is some difference between the default mesh and Mesh 2. However, making the mesh even denser only marginally changes the result. The difference in heave and vertical bending moment for the three meshes is shown in Figure 11.

It is of further interest to notice that with the refined mesh (Mesh 2 in Table 6) the ship has found a slightly different equilibrium position, indicating that the ship geometry is captured in a better way. Also, note the high-frequency noise peaks visible in the vertical bending moment in Figure 11, these are discussed further in Section 4.3.

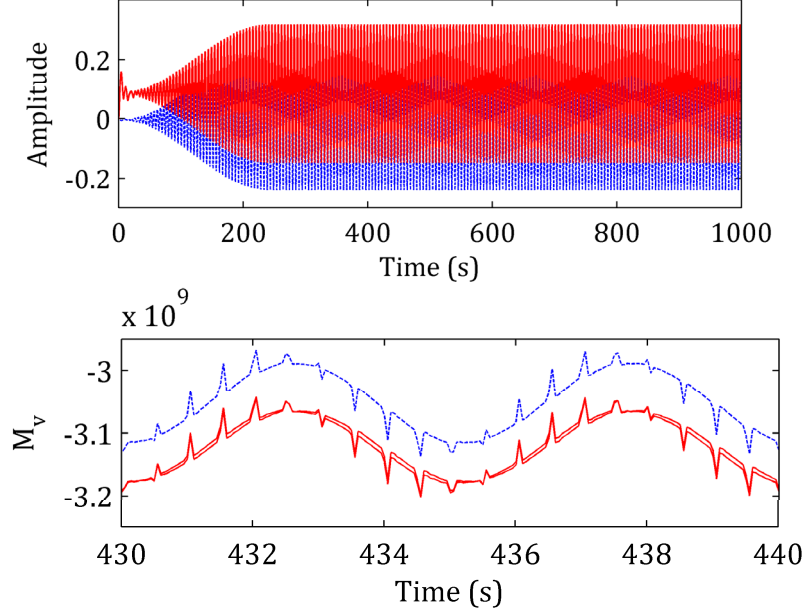


Figure 11. On the top plot, the heave response of the ship in metres using the three meshes. The blue dotted line corresponds to the default mesh and the two overlaid and very similar red lines correspond to the two refined meshes. Below, the vertical bending moment (Pa) in the mid-section for the three meshes is shown in the same colours.

4.2.2 Long term simulation stability

To investigate the stability of the solver a long simulation in a severe sea state was run. The ship response under a heading angle of 135 degrees and 8 m harmonic waves is shown in Figure 12. There is an unexpected frequency component in the roll response. The rightmost spike in the spectrum corresponds to the exciting frequency of the encountered waves given by (using Eq. (4) and a wave period of $T = 11.32$)

$$F_{\text{wave}}^n = \frac{2}{F_s T} \left(1 - \frac{2\pi U}{gT} \cos(\theta) \right) \approx 0.0124. \quad (11)$$

This peak is therefore expected - there is a constant addition of energy at this frequency. It is also shown in Figure 12 that the energy of the ship response at this frequency is constant. The leftmost peak is found at a normalized frequency of 0.0031, thus corresponding to a period of

$$T = \frac{2}{F_s F^n} \approx 32.3s. \quad (12)$$

The energy in this peak increases with time. It is therefore suspected that this second peak corresponds to an eigenfrequency of the mode which is not sufficiently damped for the energy input. Similar qualitative behaviour is observed even if the wave height is decreased, but the rate of increase in energy is lower.

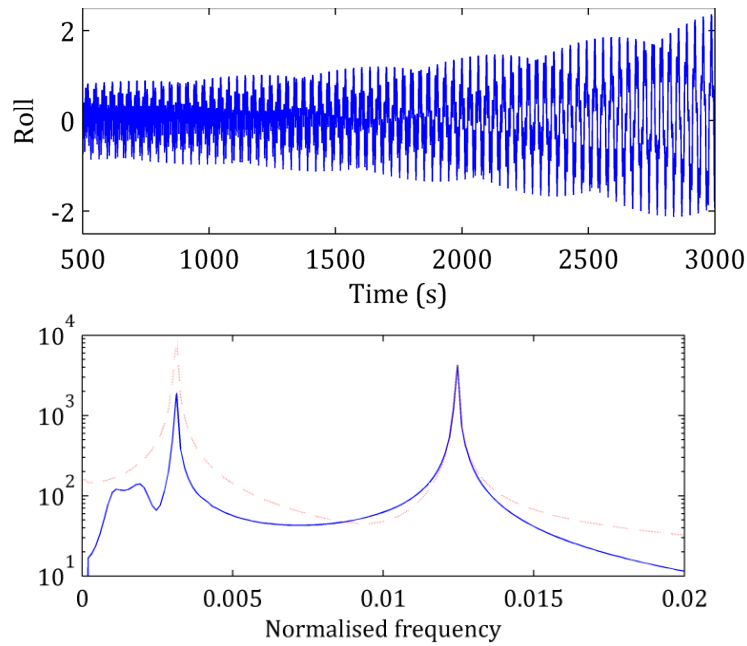


Figure 12. On the top plot, the roll angle (in degrees) of the ship over time. Under, the spectrum of the first and last 1,000 s from the 3,000 s long simulation in blue and red dotted lines, respectively.

This problem could be eliminated by increasing the extra roll damping of the ship, see for example Figure 13. An additional damping term corresponding to 5% of the critical roll damping is included, see DNV (2011c) for further description. Since no measurement data is available for calibrating the roll damping coefficient this choice of 5% of critical has been used for all further simulations.

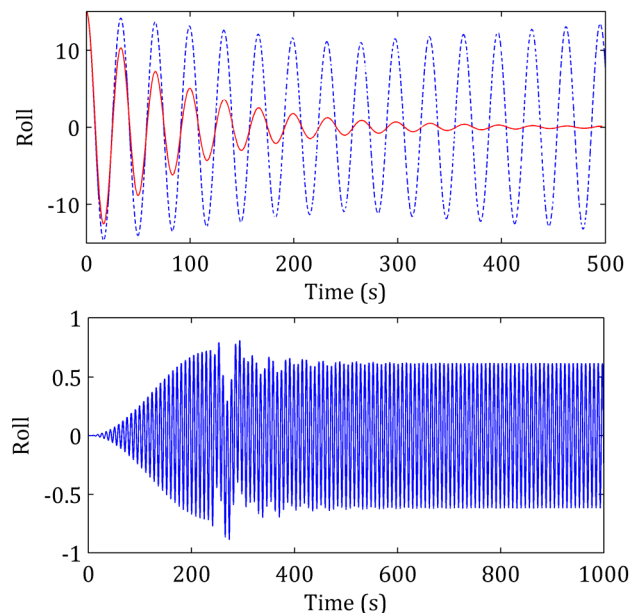


Figure 13. On the top plot, the roll angle of the ship over time without extra roll damping in dotted blue and with extra roll damping in red in a calm sea. Below, the roll response of the ship with a gradual increase in wave height during the first 200 s and extra roll damping enabled. All angles illustrated in degrees.

Having attained a stable set-up when using the linear solver the stability is investigated using the same set-up with the non-linear solver. Immediately, similar stability problems as previously described manifest.

In order to try to mitigate these effects the stiffness and the damping of the soft-spring system was increased. Figure 14 shows the response of the system when using a spring system with eigenperiods specified as 60s for surge, 30s for sway and yaw compared to the default of 120s and 60s, respectively. Hence, increasing the stiffness of the spring system is sufficient to remove the stability problem. However, 30s is an undesirably low eigenperiod of the spring system, since in following seas the encountering frequency is given by

$$\omega_e = \omega - \frac{\omega^2 U}{g} \cos(0) \approx \omega - \omega^2. \quad (13)$$

There are two ranges for which the expected response will overlap with the frequency of the spring system. Thus, for $U=10$ m/s we find that $(\omega_e \leq \frac{2\pi}{T_e} = \frac{2\pi}{30} \approx 0.2)$

$$\omega_e \leq 0.2, \text{ for } \omega \in (0, 0.276) \cup (0.724, 1.17). \quad (14)$$

Furthermore, this because the waves of periods $T \geq 22.7$ s and $5.4 \leq T \leq 8.7$ are of interest. Thus, the second of these two ranges may be problematic in following seas. For heading angles larger than 90 degrees there is no problem. This is why all further investigations have been limited to these angles.

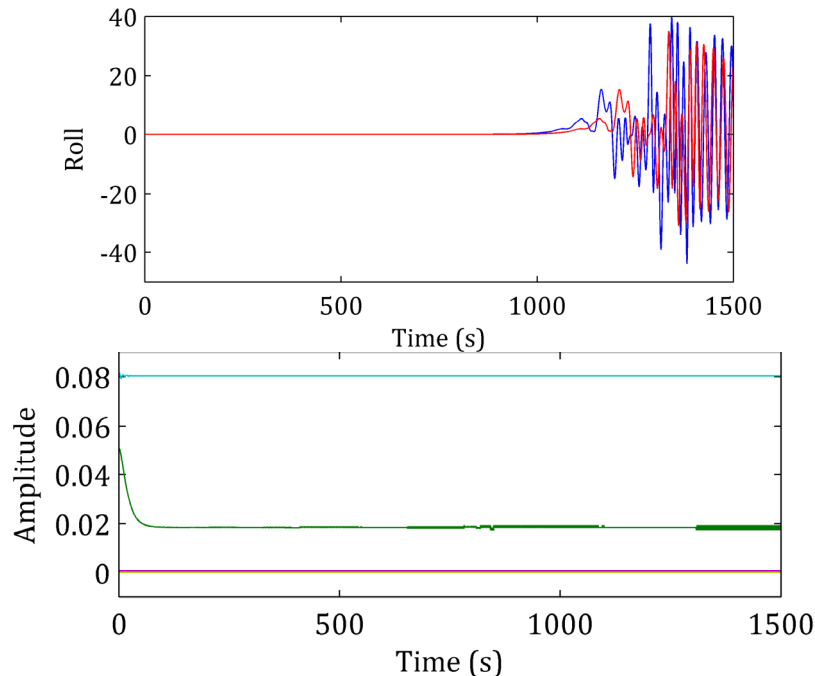


Figure 14. On the top plot, the roll angle of the ship (in degrees) over time without extra roll damping in blue and with extra roll damping in red - both cases simulated with the default spring system. Below, all motion responses of the ship with critical damping and the stiff-spring system with translational unit metres and angular unit degrees.

4.3 High-frequency noise

As previously noted and also seen in Figure 11, the force and moment calculated by the hydrodynamic solver shows an unphysical high-frequency noise of significant amplitude. Figure 15 shows further examples of these noise peaks. They are also found in the calculated pressure distribution at a sample of locations on the ship hull. These noise peaks always have a length of one sample. It should therefore be possible to filter them out from the force signals.

This section describes a method for implementing such a filtering to ensure that the desired signal still remains. This is done by

- Investigating which high frequencies the real response is expected to include when including second-order effects.
- Investigating the noise to find the minimum frequency component of the noise.
- Choosing a sampling frequency sufficiently high to separate these two frequency components.

Finally, a low pass filter is designed and applied to the noisy signal.

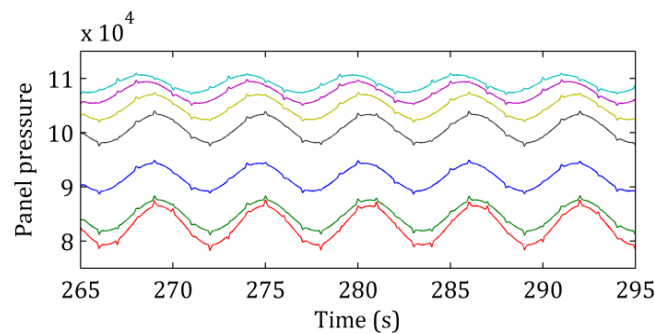


Figure 15. Pressure in Pa on a set of submerged panels on the ship hull from the hydrodynamic simulations.

However, to ensure that filtering out the noise peaks with a low-pass filter does not remove any response that should be captured, the sampling frequency must be high enough to sufficiently separate the noise from the desired information. In the non-linear hydrodynamic solver, additional terms are considered in the polynomial expansion from the numerical computation - most importantly second order terms. Now, the trigonometric identity

$$\sin(\alpha)\sin(\beta) = \frac{1}{2}\cos(\alpha - \beta) - \frac{1}{2}\cos(\alpha + \beta), \quad (15)$$

allows us to predict the frequencies of these additional terms. If we suppose that we are interested in second-order terms from an initial frequency ω_2 , then the highest frequency to be expected is $2\omega_2$ according to the identity above. Similarly, the highest frequency expected if we are interested in third-order terms would be $2\omega_2 + \omega_2 = 3\omega_2$.

Furthermore, this will also be valid for a spectrum of signals. The highest expected frequency for second-order terms would be twice that of the highest original frequency. Now, the normalized frequency of the response due to an excitation (wave) of period T at a velocity U and heading angle of θ is given by

$$F_w^n = \frac{2}{F_s T} \left(1 - \frac{2\pi U}{gT} \cos(\theta) \right) \quad (16)$$

where F_s is the sampling frequency. Assuming a minimum period of interest of 4s it is found that

$$F_w^n \leq \frac{2}{F_s T} 2.6 \leq \frac{1.3}{F_s}. \quad (17)$$

However, assuming interest only in second-order terms, the highest peak of interest may actually be found at a normalized frequency twice that, thus

$$F_w^n \leq \frac{2.6}{F_s}. \quad (18)$$

Now, to be able to find an appropriate cut-off frequency the frequencies of the noise are needed. An investigation shows that noise peaks can be found at as low normalized frequencies as 0.1 (but never lower), see Figure 16. In the two examples, the response is computed by the linear solver. The noise peaks in the response spectra indicate that all additional peaks are just caused by noise signals.

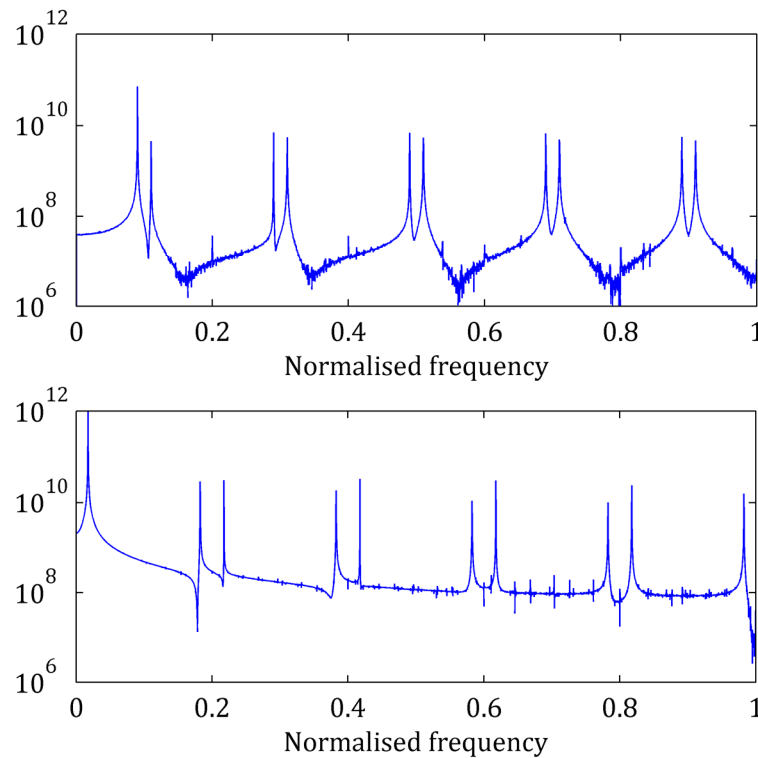


Figure 16. Spectra of vertical bending for sampling frequencies of 10Hz (top) and 20Hz (below) with harmonic seas of period 4 and 6 s, respectively.

To allow for a transition band in the filter and using the assumption of a lower noise limit of 0.1 the pass and stop band of the filter used for removing the noise were set at $F_{pass}^n = 0.08$ and $F_{stop}^n = 0.12$, respectively. Now, given Eq. (18) the sampling frequency should be at least

$$F_s \leq \frac{2.6}{0.08} = 32.5 \text{ Hz}, \quad (19)$$

to be able to fully remove all the noise. It also ensures that all second-order terms are kept. However, increasing the sampling rate also increases the computational time. Therefore, the sampling rate is set at 20Hz since this will leave all first-order components unfiltered and only filter the second-order responses of absolute maximum frequency, where a very small energy content is expected. Considering the pass band edge of $F_{pass}^n = 0.08$, this then corresponds to an actual frequency of

$$F_{pass} = \frac{F_s F_{pass}^n}{2} = \frac{20 \cdot 0.08}{2} = 0.8 \text{ Hz}. \quad (20)$$

Now, in order to find what period of encounter of second-order terms this correspond to, divide by 2 and take the reciprocal, one finds that $T_2 = 2.5$ s. Thus, the shortest wave period for which all second-order terms are guaranteed to be unaffected is $T = 5.4$ s. Almost all second-order components will also be included after filtering. Figure 17 shows a sample of a sectional force history before and after filtering. Note that this filtering significantly changes the predicted fatigue damage due to the decrease of stress cycle amplitudes. See, for example, Figure 17. With constructive noise peaks, the stress range would be increased by about 10%, creating a damage rate over-prediction of close to 40%.

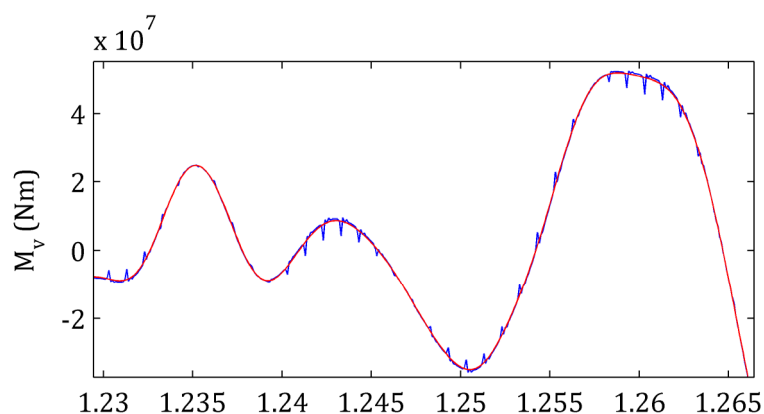


Figure 17. Vertical bending moment over time as output from solver (blue line with the small peaks) and after low-pass filter is applied (red line without small peaks).

4.4 Linear and non-linear panel methods

When computing the hydrodynamic loads using a panel method in Wasim, both linear and non-linear solvers can be chosen. Let the structural stresses be calculated by engineering beam theory. For both harmonic waves and irregular seas, the difference

in fatigue damage prediction using hydrodynamic loads computed between the linear and non-linear solvers is presented in Figure 18. It is of interest to note how the large difference in predicted damage in the harmonic case does not imply a corresponding difference in the sea states. It is also found that for small wave heights the non-linear solver actually under-predicts the damage as compared to the linear solver and that the zero crossing seemed to occur for a significant wave height of 3 m. Note that for the most common sea states on the North Atlantic the difference in damage prediction using the linear and non-linear solver is less than 10%.

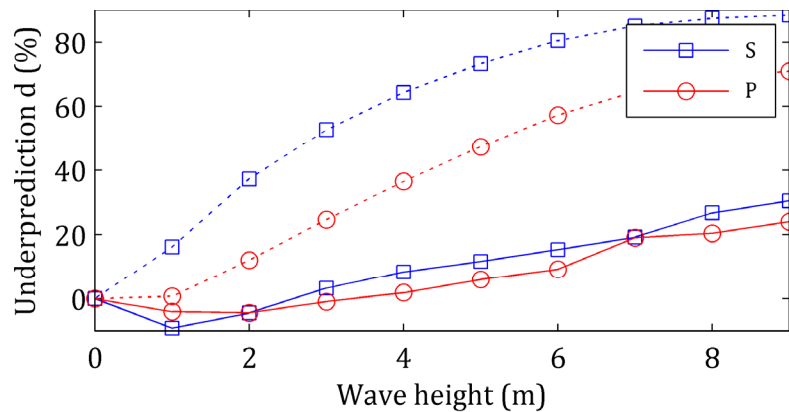


Figure 18. Under-prediction of the damage rate for the linear solver as compared to the non-linear solver in a harmonic bow sea in metres (top two dotted lines), and bow irregular seas (bottom two solid lines). The corresponding (significant) wave heights are given by the abscissa. In the legend, S and P refer to the point at the starboard and port side, respectively.

4.5 RAOs and strip theory

If the ship response is computed by the linear panel method, response amplitude operators can be obtained by correlating ship response, for example the ship motion and sectional forces etc., to the harmonic waves that the ship is subjected to. Alternatively, the RAO's can be directly computed using the strip theory in the frequency domain, which is more time- efficient.

To investigate the difference in fatigue prediction both methods have been used to perform calculations - Figure 19 shows one example of response amplitude operators from these two methods. It shows the computed response of the vertical bending moment for a ship speed of 10 m/s and heading angles of 160 and 155 degrees, respectively. Qualitatively similar behaviour with only marginal differences is observed in peak height and width.

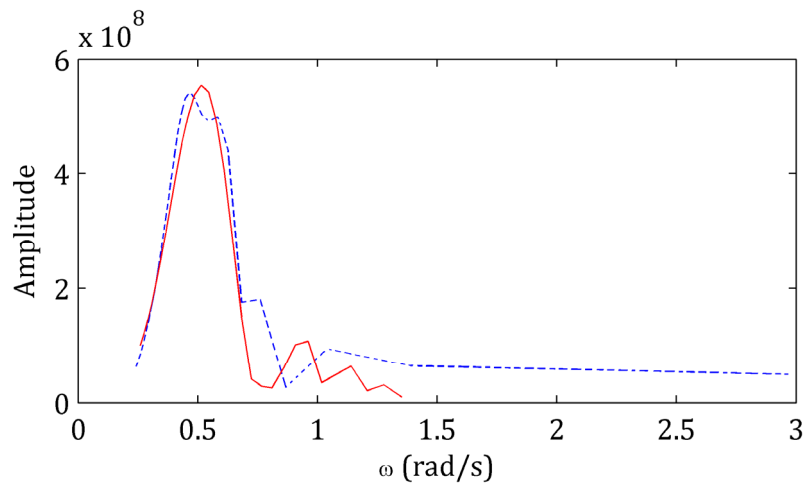


Figure 19. Amplitude of RAO for a ship speed of 10 m/s and vertical bending moment. Dotted blue line from panel methods solver and red line from strip theory solver. Heading angles of 160 and 155 degrees, respectively.

To compare how large an effect these differences have on the fatigue damage prediction, the ship response under several sea states is analysed. In all cases, the ship speed was set at 10 m/s and a heading angle of 135 was used. Figures 20 and 21 show the difference in the predicted fatigue damage for different waves heights when the RAO's are computed from the linear panel method and the strip theory. It is concluded that the overall trend is similar, but especially for low wave heights strip theory predicts larger damage than the panel method.

No attempt to match the data has been performed but the default settings in the strip theory code are used. It is likely that the results could be made to agree more by tuning of parameters. However, it is believed that this would not produce a meaningful comparison, since most often only one of the two methods is used for computing the estimated fatigue damage of a detail.

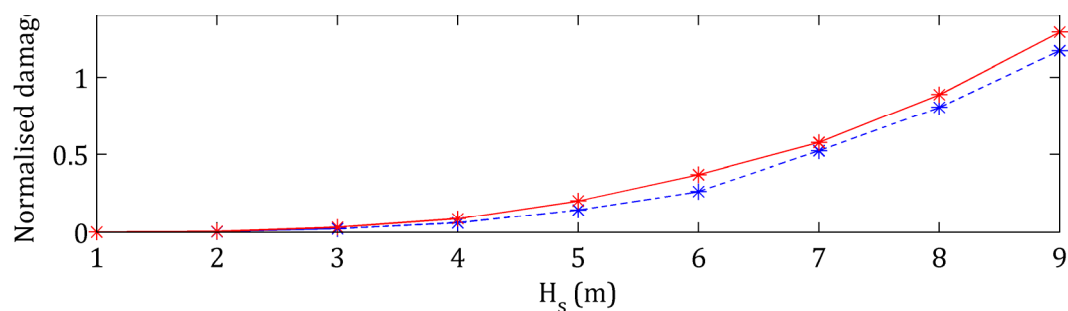


Figure 20. Normalized damage as calculated in the frequency domain from RAOs constructed from a linear panel solver (dotted blue) and strip theory (red). The narrow band approximation has been used for damage computation

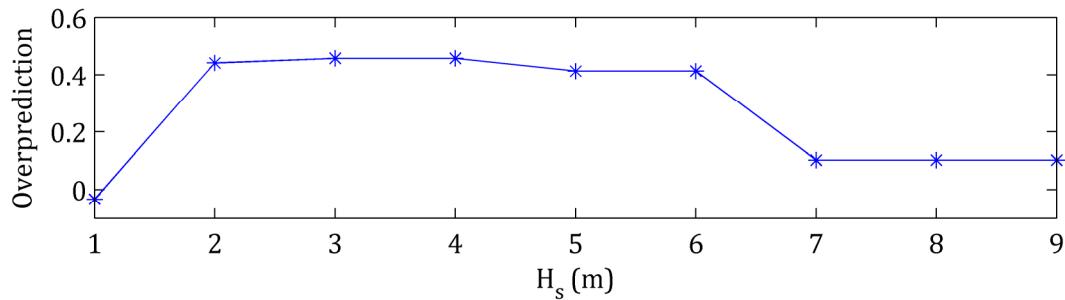


Figure 21. Over-prediction in damage for the strip theory as compared to the linear panel method over significant wave height.

4.6 Concluding remarks

It is known that there are large uncertainties involved in the hydrodynamic load analysis. These can lead to ship motion and resulting stresses differing significantly due to different computing sources, or even the same computation code with different settings. Much effort was made in finding a configuration that gives a stable and reliable solution of wave loads. Specifically the stiffness of the spring system was increased, additional roll damping was added and a significantly longer ramp period was used.

According to DNV fatigue guidelines (DNV, 2010a), a linear model of the ship response is sufficient when evaluating the fatigue damage. The performed calculations show similar results. The difference in predicted fatigue damage using a linear and weakly non-linear model is less than 20%. Furthermore, a frequency domain calculation using the RAO's from the linear panel method is sufficient as compared to the result obtained from the non-linear panel method solver (see also Section 7).

However, the damages predicted using results from the panel method solver and the frequency domain strip theory solver differ significantly. Since no empirical data is available to compare to, it is not possible to conclude which of these sets of data provide the most reliable prediction. The difference between the two methods is as large as 40%. The panel method solver has been chosen as the reference. It is partly because this method implements more advanced theory, which can capture more complex phenomena for hydrodynamic load analysis. Furthermore, the pressures on the hull are needed for computing the girder stresses using the finite element analysis.

It is of interest to note that the default option for sea state generation in the hydrodynamic panel method solver, Wasim, appears to produce a water surface that statistically does not match its expectation. Based on the linear wave theory, the water surface elevation for a given point is expected to be normal distributed. This is not the case when using the random subdivision of the wave spectrum for the selection of wave components.

Finally, a surprising artefact was found in the computed hydrodynamic response. The noise peaks found in both cross sectional moments and panel pressures indicate the presence of an error in the code. Unfortunately, these seemingly small peaks may lead to significant errors in fatigue life predictions. Actually, some examples of using this noisy output without filtering have been found by the author. Due to the noise, an

increased stress cycle amplitude of up to 15% has been found for the considered container ship in a moderate sea state. This leads to an over-prediction of fatigue damage by 52%.

5 Global structural analysis

Having acquired the hydrodynamic loads from the sea on the ship, the next step in the fatigue analysis is to evaluate their effect on the hull structure. This section tries to investigate the different options for evaluating the girder stresses due to the global loads. Additionally, the effect of the different stress contributions is investigated. It quantifies the fatigue damage caused by vertical bending, horizontal bending and warping, respectively.

Two main methods are employed. The first method calculates the cross sectional forces and moments on the ship structure. The corresponding stresses are then computed by engineering beam theory. Alternatively, the water pressure is transcribed directly onto a quasi-static FE model to calculate the loads in the structure.

This section starts with a short discussion on the sectional properties of the ship mid-section. It is followed by a description of the methodologies used for extracting sectional forces and moments on the ship structure. These are needed for correct usage of the engineering beam theory. Next, a comparison is made between the global stresses at the location of the detail between using engineering beam theory and a FE approach.

Subsequently, the longitudinal stress found in the FE model is decomposed into the components caused by axial forces, vertical bending, horizontal bending and warping using a semi-empirical method. Similarly, an additional section just forward of the engine bulkhead is chosen and the longitudinal stress is decomposed. These components are compared to the stresses predicted by engineering beam theory. It shows the importance of horizontal bending and warping compared to vertical bending for the longitudinal stress.

5.1 Cross sectional properties and forces

When comparing different methods for finding the global stress at a certain position it is important to ensure that the same structural properties are used. In particular, when comparing the stresses obtained from engineering beam theory with that from an FE computation the properties of the FE-model should be verified.

Table 7 shows the cross sectional properties of the mid-hold section as estimated using different methods. The *direct* method refers to calculating the area, neutral axis and area moments of inertia based on a mid-section drawing of the ship. These calculations are performed without any thickness reduction due to corrosion margins or compensations for effective flanges. The *beam equation* model refers to values obtained by repeating the middle hold including bulkheads to a 400m long beam and comparing the resulting deformation to the Euler-Bernoulli beam equation. The *stress distribution* method refers to finding the cross sectional properties by in least squares sense fitting lines to normal stress and position in the cross sections. For more detailed descriptions of these methods see Appendix A.

The results indicate that there is a significant difference in the cross sectional properties of the model and the drawings. There is also a large variation in the horizontal moment of inertia J_x of 17% between the two measures on the model. In the

following investigation, the mean of these values have been used when computing stresses using engineering beam theory.

Table 7. Cross sectional properties of the mid-section of the ship as calculated from drawings and measures on the FE model.

	A	z_{na}	I_v	I_h
Direct	4.56	10.01	334.6	782.4
Beam equation	4.59	-	336.3	655.1
Stress distribution	-	10.75	338.3	766.9

Having obtained values for the cross sectional properties of the ship and the FE model, there is also a need for correct cross sectional forces. In combination these allow for a comparison between stresses from the FE model and engineering beam theory. Early investigations indicated that the sectional forces outputted by the hydrodynamic simulation might be questionable. The following three sub-sections will introduce three different methods used for obtaining sectional forces from the sea state calculations.

5.1.1 Wasim

The hydrodynamic solver, WASIM, provides an option to export sectional forces and moments directly from the solver. How these are computed is not specified in the manual or any other documentation available to the author, DNV (2011c).

5.1.2 Pressure integration

Assuming that the ship is a rigid body, this is also the assumption used in the hydrodynamic solver - all forces acting on this body may be summed and should equal the mass times the acceleration of the body, according to Newton's second law. Note that inertial forces must be included for this identity to be valid since the data is available in the non-inertial (accelerating) body-fixed coordinate system.

Now, to find the cross sectional forces at any location along the ship it can be conceptually divided into two parts. One is in front of and one is aft of the cross section. Since the ship is a rigid body the forces and moments acting on one of the halves by the other may be found as the difference between the acceleration of this part and the additional external forces acting on it, given by

$$F_c = M\bar{a} - \bar{F}_{ext}, \quad (21)$$

where F_c is the force in the cross section, a is the acceleration of the ship and F_{ext} are the external forces on the half of the ship. The acceleration of the ship is available as an output for each time step from the hydrodynamic solver. Note that the inertia factor M is a 6 by 6 matrix and that both forces and acceleration have six components. The inertia matrix is also available as an output from the hydrodynamic solver.

The external force acting on the ship half is comprised of pressure forces, gravitational forces and stabilizing forces. The gravitational force is accounted for by

simple vector decomposition based on the roll and pitch of the ship. The stabilizing force is created by the spring system in the hydrodynamic. For these calculations they are obtained from the reaction forces calculated by the FE software when solving a time step given the gravity and panel pressures.

The pressure force acting on the ship half is found by integration of the panel pressures transferred from the hydrodynamic solver to the FE solver, only including the panels belonging to the considered ship half. Figure 22 shows an illustration of the pressure panels used for pressure transfer.

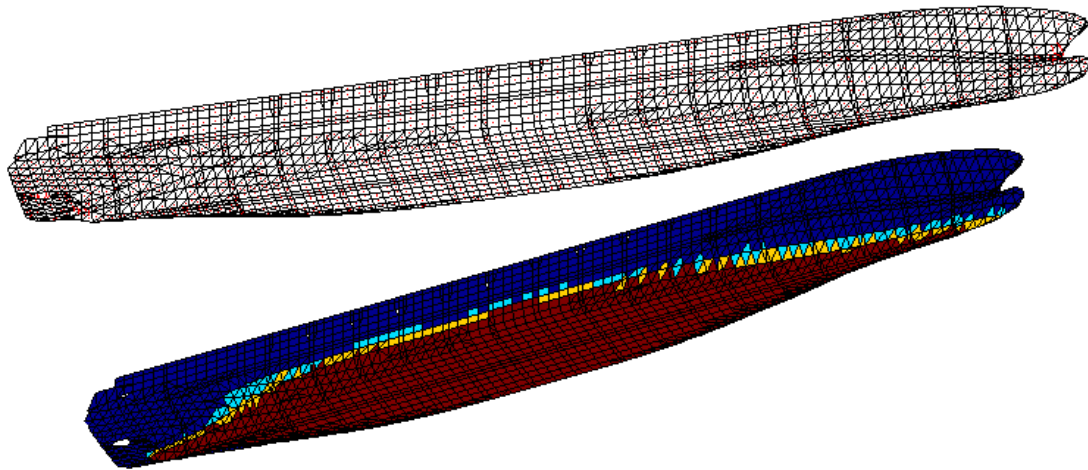


Figure 22. Pressure panels on the hull and a sample of transferred pressures in a sea state simulation where the shading represents the pressure on the corresponding element.

5.1.3 Stress integration

By using the pressure distribution and solving the FE model the stress in every element is obtained for each time step. These stresses are used for constructing a third set of cross sectional forces as described below.

Choosing the mid-section of the ship and selecting all elements intersecting this section produces Figure 23. Note that only stresses in shell elements are illustrated in this figure, but all beam elements are shown and shaded in grey.

Through the integration of stresses, longitudinal as well as shear, in shell elements in the cross section a set of forces and moments is created. This is complemented by the normal forces in all beam elements and the moments from beam elements and shell elements. A summation of forces and moments for each time step, taking care to use the correct levers and orientation of shell elements, leads to a time series of cross sectional forces and moments for the chosen section.

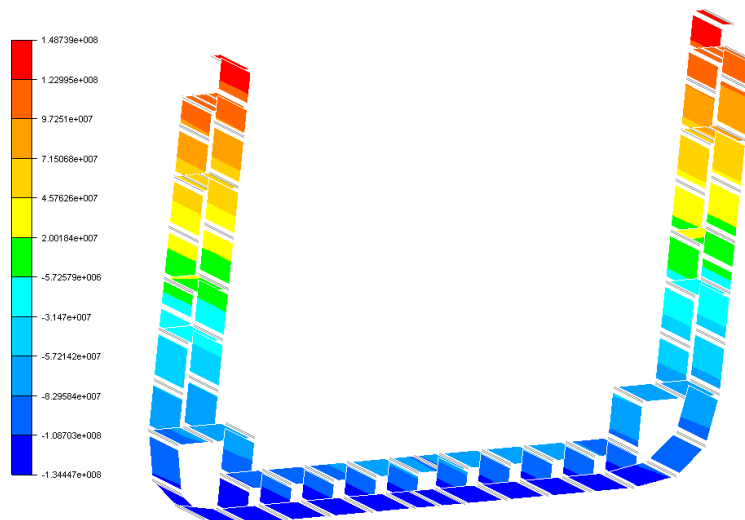


Figure 23. Longitudinal stress in all elements intersecting the mid-section of the ship.

5.1.4 A comparison of sectional forces

Three different methods for calculating the cross sectional properties have been described. This section attempts to compare them. This is done by using data from a sample case with a heading angle of 125 degrees and an 8m significant wave height. This sea state is first solved using the hydrodynamic solver, extruding the cross sectional moments and subsequently performing a quasi-static FE calculation on the ship.

Two measures, i.e. integrating all the pressures on the front or aft half of the ship, can be used for the pressure integration. Provided that all forces are accounted for the two measures should be equal to each other. Figure 24 shows that integrating from bow and stern produces very similar measures when including the reaction forces such as from the soft-spring system. Furthermore, the cross sectional moments obtained by stress integration of the section in the FE model agree well with the moments obtained by pressure integration. This is as expected and indicates that the two methods are implemented correctly. Note that disregarding any of the components, such as inertial or gravitational (even in the ship's lengthwise direction, where the component of gravity is very small due to limited pitch motion) forces in the pressure integration, leads to completely different results from the stress integration method.

However, the sectional moments obtained from the hydrodynamic solver does not agree with the results obtained by either of the two methods implemented by the author. Notice both the significantly increased amplitude and the difference in local peaks and troughs.

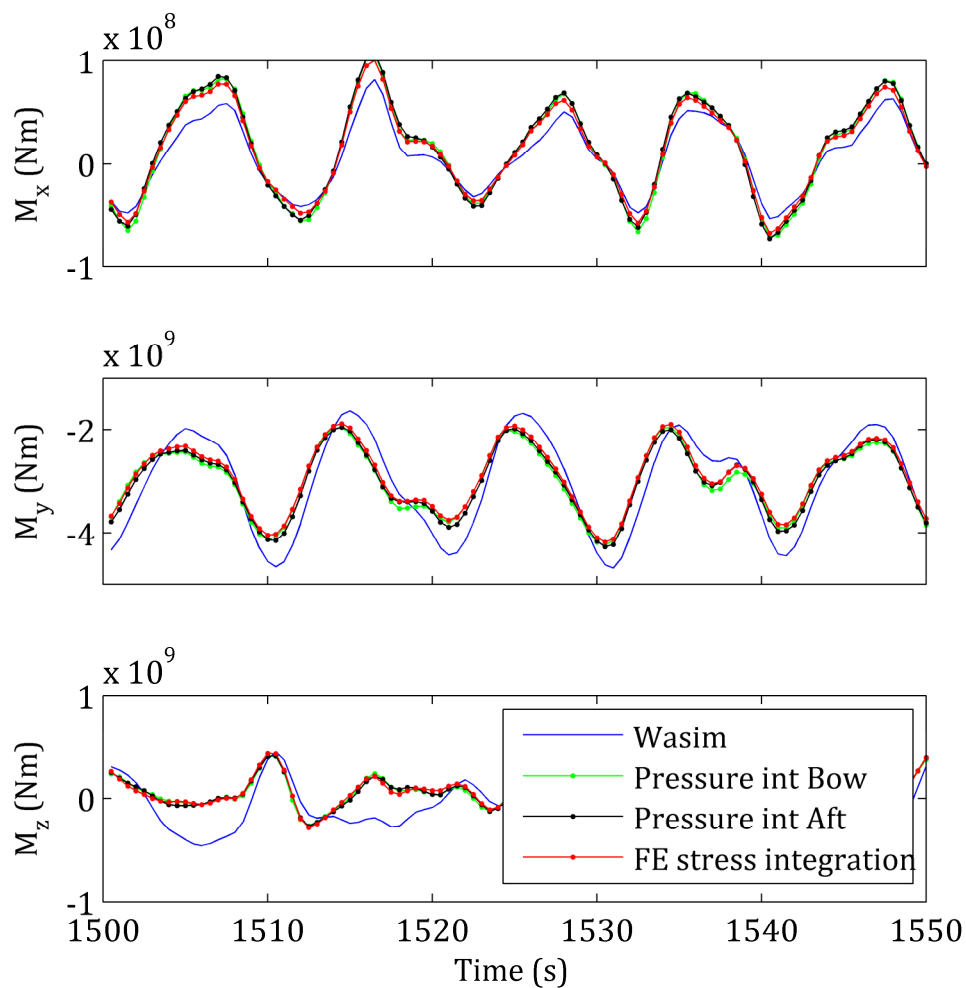


Figure 24. Calculated cross sectional moments from the three methods over time in an 8m significant wave height sea state simulation. Pressure integration is here performed disregarding the effects of reaction forces.

To investigate how the forces and moments are calculated in the hydrodynamic solver the pressure integration was redone, now ignoring the components stemming from reaction forces such as spring and rudder forces. The results for the same time series are presented in Figure 25.

First note that the cross sectional moments integrated from bow and stern no longer match, since additional forces not accounted for now exist on the ridged body. Next, notice that the moments as integrated from the bow now well match the direct output from the hydrodynamic solver. This indicates that the solver uses the method described as pressure integration, but does not consider the forces from the spring system, etc., and integrates the pressures on the bow half of the ship.

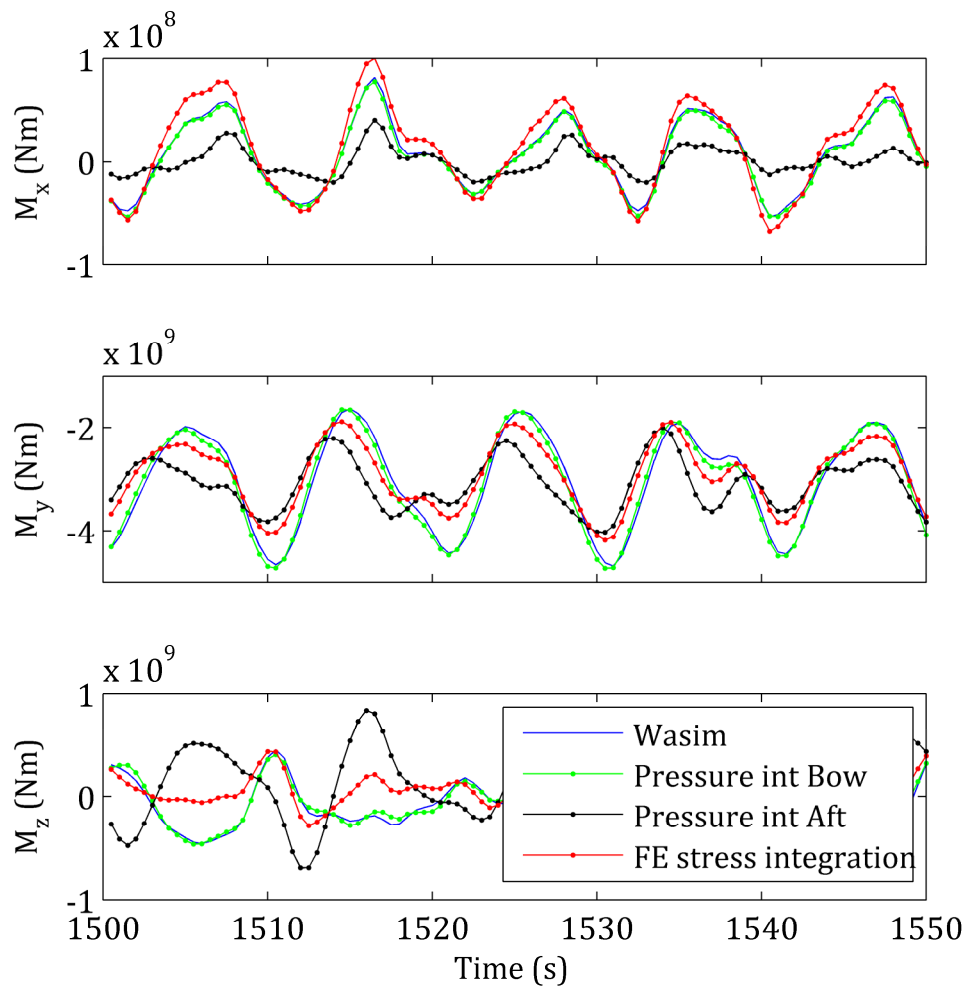


Figure 25. Calculated cross sectional moments from the three methods over time in an 8m significant wave height sea state simulation. Pressure integration is here performed including the effects of reaction forces.

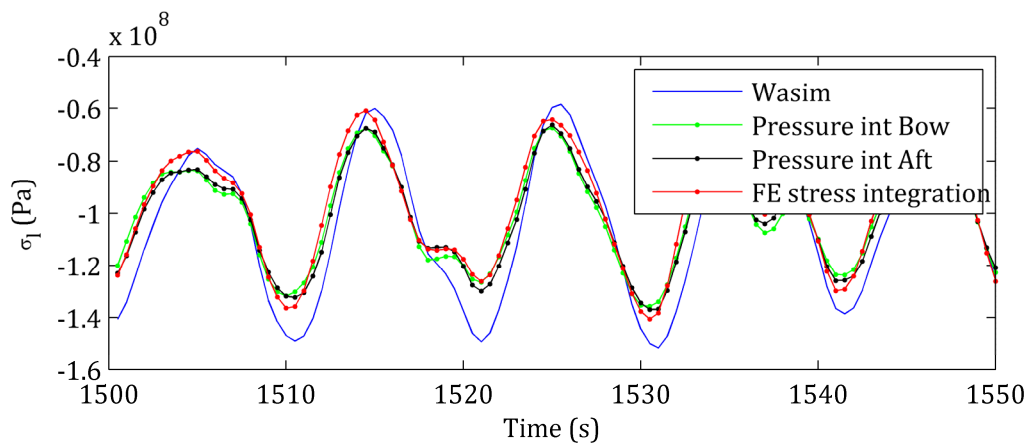


Figure 26. Longitudinal stress in detail as calculated using the engineering beam theory with horizontal and vertical bending for different measures of cross sectional moments. Stress from the FE model is plotted as a reference.

In order to try to quantify the effect these differences in procedure would create in a fatigue measure, Figure 26 was produced. Here, the global longitudinal stress at the detail, as extracted from the beam element corresponding to the stiffener, is compared to the longitudinal stress as calculated using the engineering beam theory with vertical and horizontal bending for the three sets of cross sectional forces being calculated. The pressure integration is performed including the effects of reaction forces.

As expected, the results from stern and bow integration agree very well, and they agree reasonably well with the stresses from the FE model. The differences may be explained by longitudinal stresses due to torsion and these are included in the FE model. The differences are, however, reasonably small and the amplitudes between FE data and pressure integration are similar. However, the longitudinal stress calculated using the engineering beam theory and the moments from the hydrodynamic solver show considerably larger stress ranges and different local details in the stress history. The difference in stress amplitude is approximated to about 40%.

Despite these differences the cross sectional moments directly from the hydrodynamic solver will subsequently be used for fatigue damage computations. This choice is made since this is the data typically used by the end user, and this is the comparison that is to be made.

5.2 Beam theory and FE comparison

Table 8 shows the difference between the calculated damage rate using the global FE model and engineering beam theory for a sea state with $H_s = 7.5\text{m}$ using the non-linear panel solver for the hydrodynamic loads. It is found that the FE calculations predict significantly less damage than engineering beam theory. Furthermore, there is a difference between the starboard and port side, indicating that there is a difference in either the horizontal bending moment or torsion. Note that torsion was not accounted for in the engineering beam theory calculations.

Table 8. Over-predicted fatigue damage rate using engineering beam theory with vertical and horizontal bending moment and WASIM cross sectional moments as compared to the FE solution.

Ship side	Starboard	Port
Fatigue over prediction	46%	271%

One explanation for this difference may be the usage of incorrect sectional moduli, leading to prediction of erroneous stresses and the resulting fatigue damage. To investigate this, the wave loads applied on the ship structure were directly transferred from the hydrodynamic analysis.

In order to further understand the difference of the computed structural stress between the FE analysis and the engineering beam theory, we assume that there is a linear relationship between the sectional forces and the longitudinal stress through a coefficient vector C

$$\sigma_x = CF. \quad (22)$$

where the sectional forces F come from the hydrodynamic software and the longitudinal stress σ_x is obtained from the FE calculation. In general, F is a vector consisting of six components, three forces and three moments. However, using the engineering beam theory assumption that the longitudinal stress is independent of forces orthogonal to the cross section, and the fact that the axial force is small, the sectional force vector may be taken as:

$$F = [M_x, M_y, M_z]^T. \quad (23)$$

Regressing for C in the least squares sense from $H_s = 7.5$ m for the two sides leads to

$$\begin{aligned} C^S &= [-0.216, 0.028, -0.0008] \\ C^P &= [-0.360, 0.029, -0.0079] \end{aligned} \quad (24)$$

The resulting stress calculated as CF corresponds well to the stress history obtained from the FE calculation, see Figure 5. This leads to a small prediction difference in fatigue damage compared to the FE calculation of 1% and 6%, respectively.

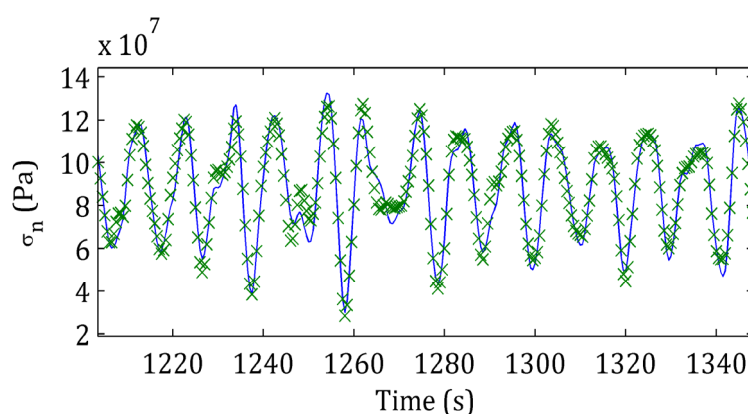


Figure 27. Stress history from sectional loads combined using regression represented as a solid line. Sample points from the FE-solution marked with crosses. The history is for the starboard side in a sea state described by $H_s = 7.5$ m.

Only using six random time samples for each regression rather than the entire series and using 500 trials, leads to similar coefficients with the following standard deviations:

$$\sqrt{\text{Var}[C^S]} = [0.111, 0.001, 0.012]. \quad (25)$$

Thus, the value of the vertical section modulus appears deterministic, whereas there is a great variation in the regressed values for warping and horizontal bending modulus. Using these different regressed values leads to coefficients of variation in damage over-prediction of 0.32 and 0.29 for the starboard and port side, respectively. This indicates that the changing moduli for warping and horizontal bending largely affect the fatigue results.

Note that the reciprocal of the coefficients in the $C^{S,P}$ matrices corresponds well to the sectional modulus for vertical bending $35.7 \approx 29.9$, while the magnitude is clearly wrong for the horizontal bending, $-1250 \neq -50.3$. Furthermore, both warping and horizontal bending stresses are expected to contribute symmetrically but with opposite signs to the starboard and port sides; this is clearly not the case here.

Hence, there is still a discrepancy between the stress predicted by the engineering beam theory and the FE analysis above, indicating that the reason for the difference is not only found in the usage of the wrong section moduli. However, the results from Section 5.1 indicate that the sectional forces exported from the panel solver do not match the sectional moments that the structure in the FE model is subjected to, explaining the difference above.

However, using the coefficients regressed above for the same ship in different sea states described by different heading angles and wave heights indicate that the predicted fatigue damage for these different sea states using the engineering beam theory and the moments from the panel solver matches well with those found from an FE analysis.

In order to investigate the effect of the different contributions to stress the decomposition of the stress found in the FE model into components stemming from vertical, horizontal bending and warping are next looked into.

5.3 Component decomposition

To try to quantify how large a proportion of the accumulated fatigue damage is caused by stresses due to vertical, horizontal bending and torsion, the longitudinal stress in the detail needs to be divided into parts resulting from the different components. When computing the longitudinal stress using the engineering beam theory and sectional moments this subdivision is straight- forward.

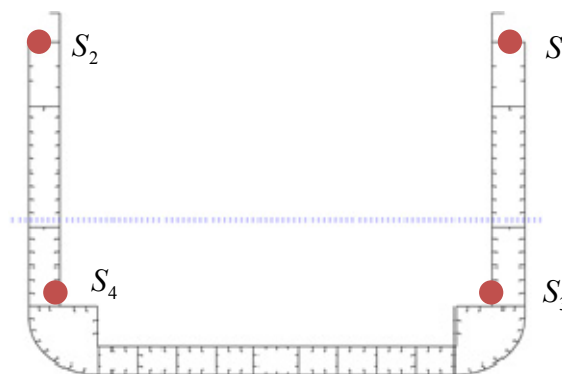


Figure 28. Location of the stress read-out points in the mid-ship cross section. Note that no location is subjected to additional local stress components such as plate bending.

However, given stresses measured from an actual ship, or in this case given the stress field of the ship FE model, the process is slightly more involved. Using the methodology presented by Storhaug and Moe (2007) this decomposition may be performed by measuring the stresses in the four locations labelled S_1 through S_4 in

Figure 28. These locations are chosen because full-size stress data is available for them. For these locations, symmetrically distributed in the cross section, we know that the contribution from both horizontal bending and warping are opposite on the two sides. By further using the data for ratios between sectional moduli for the different locations, a relationship between the stress contribution from horizontal bending, vertical bending, torsion and axial forces in one location and the total stresses measured in the other points. This is exemplified in the equation above where σ_i denotes the corresponding longitudinal stress contribution for the detail on the starboard side.

$$\begin{bmatrix} S_1 \\ S_2 \\ S_3 \\ S_4 \end{bmatrix} = \overline{A} \begin{bmatrix} \sigma_V \\ \sigma_H \\ \sigma_W \\ \sigma_A \end{bmatrix} \quad (26)$$

Note that in this relationship the first row is composed of four 1's since S_1 is the stress measured at the detail and this is simply the sum of the contributions from the four contributions. By using the section moduli for the four locations and inverting the relation the following equation is obtained, Storhaug and Moe (2007)

$$\begin{bmatrix} \sigma_V \\ \sigma_H \\ \sigma_W \\ \sigma_A \end{bmatrix} = \begin{bmatrix} 0.343 & 0.343 & -0.343 & -0.343 \\ 0.268 & -0.268 & 0.255 & -0.255 \\ 0.232 & -0.232 & -0.255 & 0.255 \\ 0.158 & 0.158 & 0.343 & 0.343 \end{bmatrix} \begin{bmatrix} S_1 \\ S_2 \\ S_3 \\ S_4 \end{bmatrix}. \quad (27)$$

To check the applicability of this relationship, the stress contribution in the detail from vertical and horizontal bending is computed and plotted in Figures 29 and 30. Here, a full-ship FE solution is performed on the results of a sea state ship simulation and stresses in beam elements corresponding to the four locations S_i are extracted, and these extracted stresses are multiplied by the matrix above to provide one measure of the stress contributions. Additionally, the longitudinal stresses due to the two bending components are calculated using the engineering beam theory and the sectional moments as calculated by the hydrodynamic solver and pressure integration method described earlier.

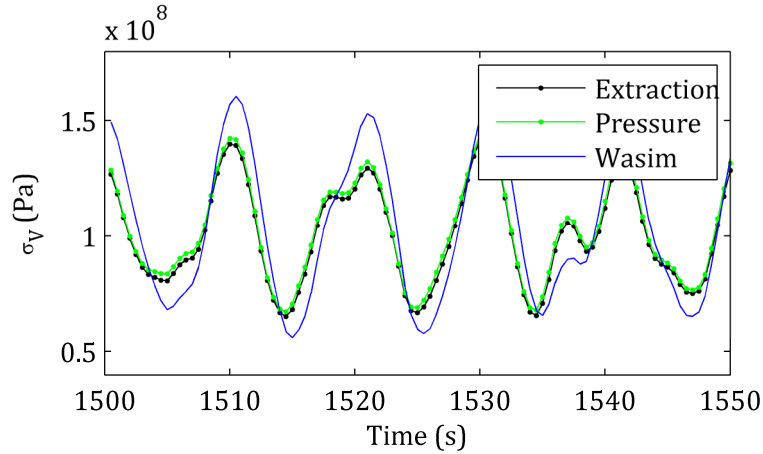


Figure 29. Longitudinal stress contribution from vertical bending in the detail on the starboard side as calculated from stresses extracted from the full-ship FE model as well as using the engineering beam theory and the sectional moments from pressure integration and from the hydrodynamic solver Wasim, respectively.

The agreement between the contributions as calculated from the extracted stresses matches the contributions calculated using the engineering beam theory and the pressure integrated sectional moments very well, indicating that this decomposition method works well. Note, however, the relatively great difference found in the contribution as calculated using the sectional moments direct from the hydrodynamic solver, further indicating that these are not reliable. The contribution from warping is not shown since no good measure on the bi-moment for the location has been possible.

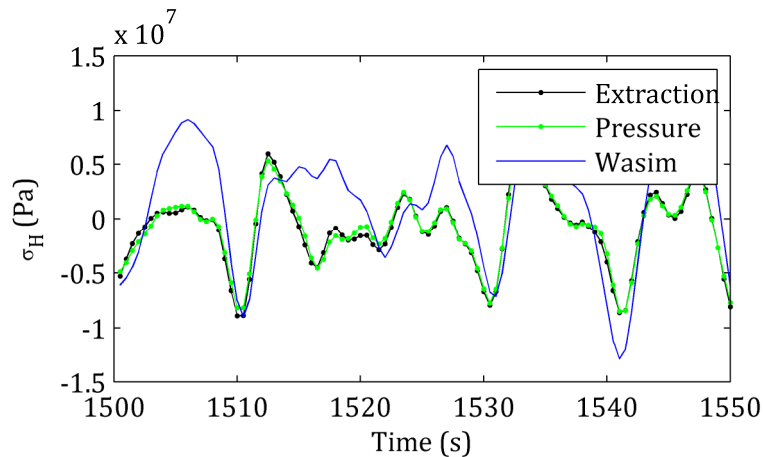


Figure 30. Longitudinal stress contribution from horizontal bending in the detail on the starboard side as calculated from stresses extracted from the full- ship FE model as well as using the engineering beam theory and the sectional moments from pressure integration and from the hydrodynamic solver Wasim, respectively.

Figure 31 shows the time history of the contributions from the four components (mean value subtracted) for the considered detail on the starboard side (S_1). It is to be observed how the variation in stress due to the axial force is very small, indicating

that the assumption of ignoring its fatigue contribution is correct. It is further interesting to observe how the contributions from torsion and horizontal bending appear to be out of phase and interfere destructively. In fact, for all cases studied this appears to be true, checked by investigating the minimum lag for the cross correlation between the two signals always being found to be zero or very close to zero. See, for example, Figure 32 for an illustration of the correlation of the two signals as a function of the time offset.

A similar set of four locations and the corresponding transformation matrix was constructed for a cross section 68 m in front of AP, or 8 m forward of the engine bulkhead. The two deck details chosen for this section correspond to the same stiffener as in the mid-section, and for the starboard stiffener the component extraction is given by

$$\begin{bmatrix} \sigma_V^{aft} \\ \sigma_H^{aft} \\ \sigma_W^{aft} \\ \sigma_A^{aft} \end{bmatrix} = \begin{bmatrix} 0.362 & 0.362 & -0.362 & -0.362 \\ 0.268 & -0.268 & 0.263 & -0.263 \\ 0.237 & -0.237 & -0.263 & 0.263 \\ 0.139 & 0.139 & 0.362 & 0.362 \end{bmatrix} \begin{bmatrix} S_1^{aft} \\ S_2^{aft} \\ S_3^{aft} \\ S_4^{aft} \end{bmatrix}. \quad (28)$$

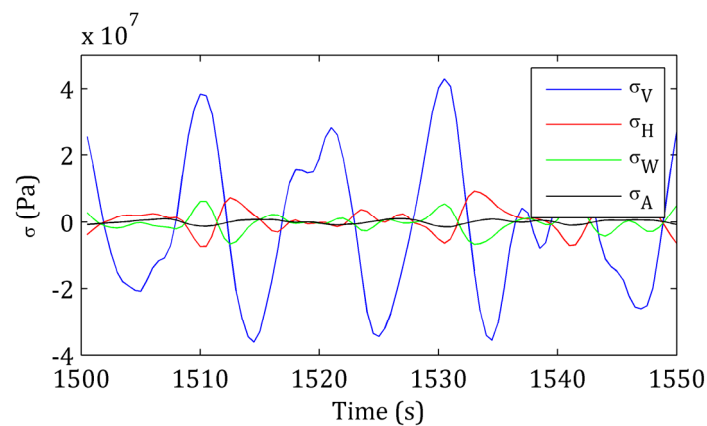


Figure 31. Time series of longitudinal stress contributions as calculated using the four extracted stresses (mean values of the signals subtracted) from a sea state simulation.

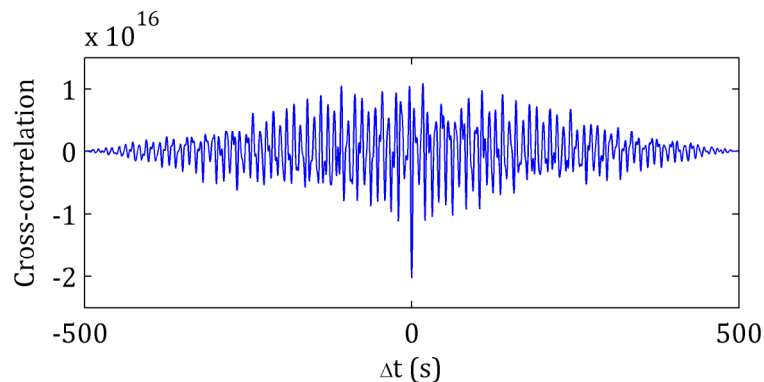


Figure 32. Cross correlation between stress contribution from warping and horizontal bending as a function of the time lag between the two signals. The minimum is found at a 0 time delay.

5.4 The effect of horizontal bending and torsion

To investigate the importance of the different contributions to fatigue damage, the decomposition of longitudinal stress described in the previous section is used for several different sea states. For all investigations in this section, sea state simulations are performed using the non-linear solver with settings as described in Section 4. The hydrodynamic pressures are transferred and the full-ship FE model is solved for a 500s long part of this simulation. The resulting FE solution is used for extracting the longitudinal stresses in the read-out points.

Nine different sea states are chosen with wave heights ranging from 2 m to 6 m and heading angles between 160 and 90 degrees. Head sea operations are not investigated. To illustrate that only one side of the ship needs to be investigated based on the odd symmetry for horizontal bending and warping contribution, Figure 33 shows the total stress in the deck detail for the starboard and port side as well as the stress when the contribution from warping and horizontal bending are subtracted, respectively. It is to be observed how the positive contribution on one side corresponds to a negative one on the other, indicating that a fatigue over-prediction on the starboard side will correspond to a match under-prediction of the port side and vice versa.

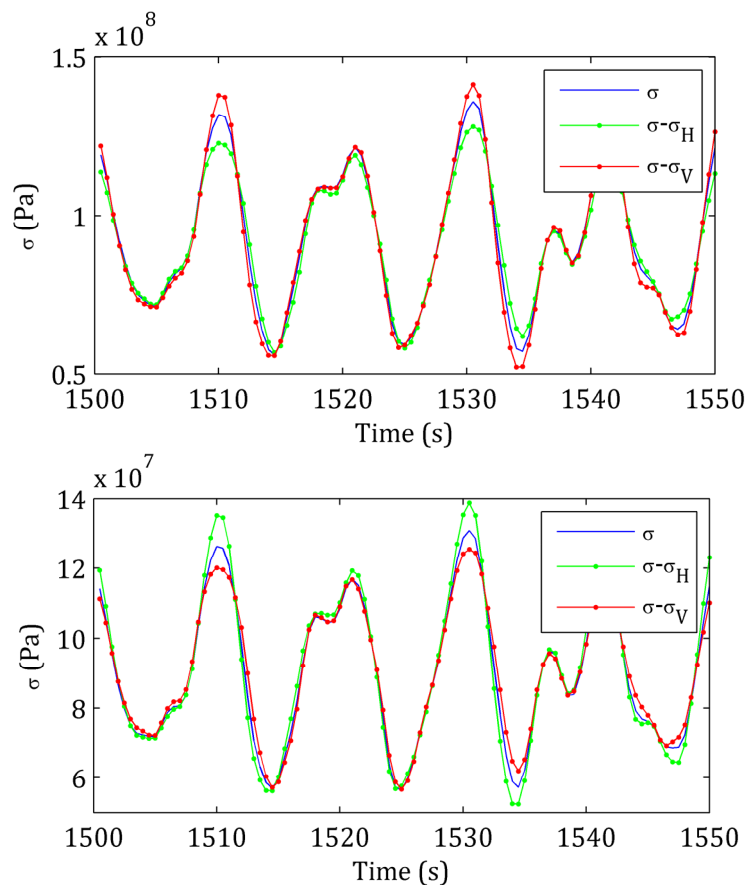


Figure 33. Stress history for the deck details of the starboard (left figure) and port (right figure) sides for total longitudinal stress σ as well as longitudinal stress subtracting the contributions from horizontal bending and warping, respectively.

Table 9 shows the standard deviation of the longitudinal stresses due to the four components for three different heading angles. As previously concluded, the variability and thus fatigue contribution for the axial force is minimal. It is further noted that, as expected, the amplitude of the variations of stresses from horizontal bending and warping are significantly less for the case of almost head sea. Also note that the amplitude in all the contributions as compared to that of the total is larger for 125 degrees than for 90 degrees.

Table 9. Standard deviation of longitudinal stress from the four components in a 2 m significant wave height sea state. All values normalized against the standard deviation of the full longitudinal stress.

θ	$std(\sigma_V)$	$std(\sigma_H)$	$std(\sigma_W)$	$std(\sigma_A)$
90	0.93	0.41	0.29	0.05
125	1.11	0.49	0.39	0.04
160	1.04	0.14	0.13	0.03

Instead, the damage rate as calculated using the engineering beam theory from the sum of different sets of stress contributions are calculated and presented in Table 10. Here, the damage from just vertical bending, everything but horizontal bending and everything but warping, and the correlation between the stress from warping and horizontal bending is presented for the detail on the starboard side.

Again, a clear correlation between horizontal bending and warping stresses exists for this location. Investigating the damage calculated by just using the vertical bending moment indicates a relatively good agreement, particularly for the 160- degree case close to head sea operations. However, for some cases, 125 degrees in particular, including just horizontal or vertical bending moment leads to significant errors in fatigue damage prediction. For example, for this mid-section detail an under-prediction of 60% is found when ignoring the warping stresses (2 m waves, 125 degrees), explained by the destructive interference between horizontal bending stresses and vertical bending stresses. An illustration of this case is shown in Figure 34, where the different combinations of components are plotted.

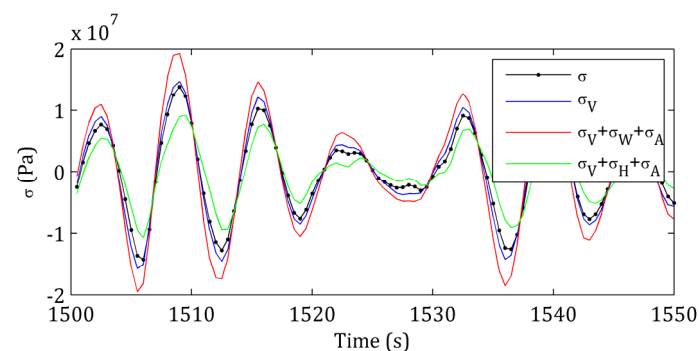


Figure 34. Time history of longitudinal stress in detail on the starboard side mid-section. The black line shows the total longitudinal stress and the other three lines show the stress when only including the corresponding components. Data extracted from an FE model run in a 2 m significant wave height sea state with a heading angle of 125 degrees.

Table 10. Damage for the starboard detail in the mid-section as calculated using the indicated stress components divided by the damage rate from the sum of all components. The rightmost column shows the correlation between the stress due to horizontal bending and warping

H_s	θ	σ_V	$\sigma_V + \sigma_W + \sigma_A$	$\sigma_V + \sigma_H + \sigma_A$	$corr(\sigma_H, \sigma_W)$
2	90	0.81	0.55	1.68	-0.96
2	125	1.29	2.64	0.40	-0.96
2	160	1.10	1.28	0.80	-0.94
4	90	0.74	0.55	1.80	-0.96
4	125	1.36	2.74	0.40	-0.97
4	160	1.10	1.26	0.82	-0.93
6	90	0.76	0.60	1.82	-0.96
6	125	1.34	2.47	0.47	-0.96
6	160	1.13	1.24	0.85	-0.97

Table 11 shows a similar table, but here for the detail in the aft cross section just in front of the engine bulkhead. Note how the correlation between horizontal bending and warping is less pronounced there and how the damage prediction using just a vertical bending moment is considerably less conservative than for the mid-section. This may be explained by the relatively larger amplitudes of the stress due to horizontal bending and warping. Additionally, these two components are no longer of as similar magnitude as previously indicated, see also Figure 35.

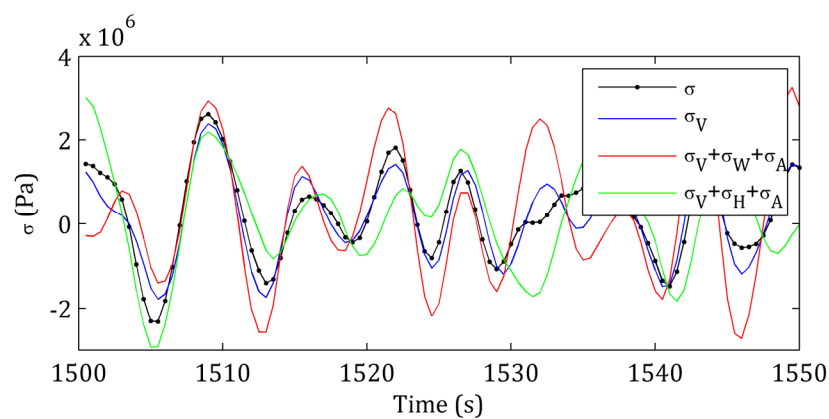


Figure 35. Time history of longitudinal stress in detail on the starboard side aft section. The black line shows the total longitudinal stress and the other three lines show the stress when only the corresponding components are included. Data extracted from an FE model run in a 2 m significant wave height sea state with a heading angle of 125 degrees.

Table 11. Damage for the starboard detail in the aft section as calculated using the indicated stress components divided by the damage rate from the sum of all components. The rightmost column shows the correlation between the stress due to horizontal bending and warping

H_S	θ	σ_V	$\sigma_V + \sigma_W + \sigma_A$	$\sigma_V + \sigma_H + \sigma_A$	$corr(\sigma_H, \sigma_W)$
2	90	0.79	3.06	0.82	-0.94
2	125	0.61	0.29	2.23	-0.68
2	160	0.66	0.59	1.31	-0.65
4	90	0.68	3.17	0.98	-0.92
4	125	0.63	0.27	2.40	-0.69
4	160	0.66	0.57	1.31	-0.64
6	90	0.66	2.73	0.99	-0.91
6	125	0.63	0.20	2.86	-0.76
6	160	0.69	0.59	1.37	-0.67

Figure 36 shows a summary of how the calculated damage changes by including different components for the two sections considered and the different sea states. It is concluded that using all components as compared to just vertical bending may produce as high as 64% more damage for the considered cases.

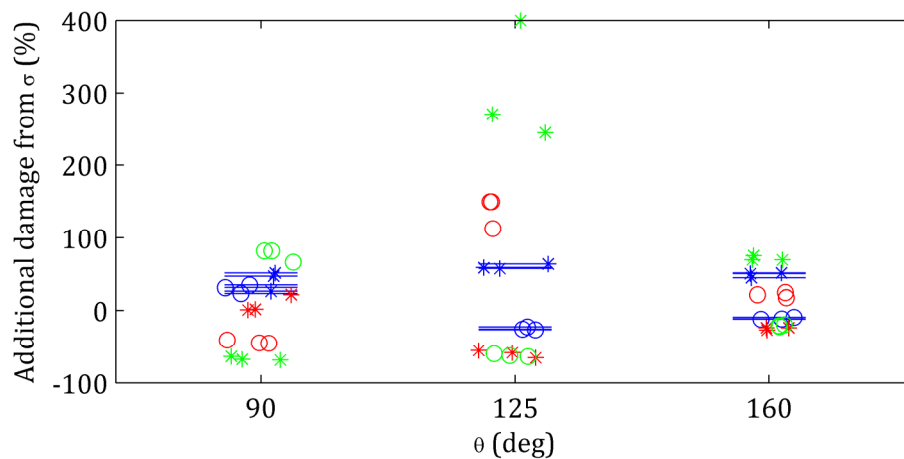


Figure 36. Additional fatigue damage obtained by using full longitudinal stress in the starboard deck detail for mid-section (points marked with *) and aft section (points marked with o), respectively. Blue points correspond to just using a vertical contribution, green to subtracting the horizontal bending contribution and red to subtracting the warping contribution.

However, by using the contribution from vertical bending and horizontal bending while excluding the stress due to warping the error in the prediction is even larger,

and in some cases an additional 150% damage may then be found by also including warping. These large variation are found for heading angles of 125 degrees. Observe, however, that even larger errors are found by excluding the horizontal bending contribution and including warping. This may be uncommon, but, due to a shift of signs to the port side, damage differences this large might be found here by excluding warping.

5.5 Concluding remarks

It is concluded that the fatigue contribution from axial forces is marginal and disregarded. However, contributions from horizontal and vertical bending are found to be substantial and should not be disregarded. For the mid-sectional detail these two contributions, however, interfere destructively and the damage estimation found by just using vertical bending is accurate to within about 25%.

Nevertheless, due to the high correlation and out-of-phase behaviour between the horizontal bending and warping contributions, large errors are found when computing the fatigue damage due to the combined effect of vertical and horizontal bending. The actual damage is found to be 150% more severe for some cases, and results indicate that there may be a situation where the difference is even greater. Even for the mid-section where the warping effect is commonly considered to be small, extra damage of above 100 % is found when including the warping effect as compared to just including vertical and horizontal bending.

Thus, the results clearly indicate that when considering fatigue damage, an approximation using just vertical bending may under certain circumstances be accurate enough. However, if horizontal bending is accounted for so need warping be to not risk unacceptably large errors.

Furthermore, these results are all found in the deck area where the contribution from vertical bending is expected to attain maximum value. Even greater differences are expected if a detail further down along the side of the hull is considered where horizontal bending and warping contributions may still retain a similar amplitude as in the deck. Despite this, this may be of less significance since the largest stress variations are expected to be found in the deck area due to the significantly greater amplitude of the variations in stress due to vertical bending as compared to the other two components.

It is of interest to notice the difference between the sectional forces and moments as exported by the hydrodynamic solver Wasim and by the two methods developed during this thesis, especially how the FE results match the sectional moments calculated here. As previously stated, this difference is due to the handling of the residual forces from, for example, the spring system. The way they are handled by the developed pressure integration method matches the FE model and therefore necessarily they provide a better match. It is hard to conclude which method better matches reality. Ignoring these forces as done by Wasim leads to an unbalanced force equation which is not physical. However, including the reaction forces leads to point loads on the hull structure that create additional moments in the section that would normally not be present.

However, the most important conclusion is the lack of reliability these results indicate. In one case, using the two different sets of sectional moments produce as much as a 40% difference in stress amplitude, corresponding to a difference in fatigue damage of 170%.

This great difference also explains the substantial difference found between the fatigue damage calculated using the engineering beam theory and the FE solution in Section 5.2, since the sectional moments from Wasim were used. Additionally, just vertical and horizontal bending were included.

The difference in the sectional moments may also indicate why the regressed matrix in Section 5.2 does not match the expected sectional properties. Unfortunately, due to time constraints there has not been time to repeat this investigation with a different set of sectional moments.

6 Local structural stress analysis

In a beam with a constant cross section and no defects a uniform stress distribution is expected under longitudinal load. However, defects or geometrical changes can lead to changes of the stress field. This will cause the so-called stress concentrations. One such example of stress concentration is the considered detail in this thesis, shown in Figure 6. The stiffener is a long slender beam with a constant cross sectional geometry, disregarding manufacturing imperfections. However, at the location where the beam is connected to the bracket there is a sudden increase (the bracket) in the cross sectional area and this leads to stress redistribution. Correspondingly, the stress will increase in the region around the corner.

In the previous sections, the global girder stress, i.e. the stress in the stiffener, was computed. This section investigates the local structural stress (hot-spot stress) in the detail, given the global load using a stress concentration factor methodology. First, the terminology and the methodology for evaluating the stress concentration based on the class guidelines is presented.

This is followed by investigating the difference in stress concentration found using the different options for element types and sizes allowed by the class rules. The effect of including or not including the deck plating is checked as well as the difference caused by using an L- shaped stiffener instead of a flat plate.

Finally, the stress concentration found in the detail when located in the hull is investigated using a displacement-driven sub- modelling approach.

6.1 Local stress evaluation methodology

In an unchanged beam, the stress calculated from, for example, the engineering beam theory is often called the nominal stress. In the areas with structural discontinuities, the structural stress becomes different from the nominal stress due to the effect of the geometrical change. In the fatigue assessment, it is often related to the hot-spot stress or geometric stress. The notch stress is the total stress at the root, including both stress increase due to the connection and weld geometry as well as local effects due to the weld toe, see Figure 37 for further illustration, DNV (2010a).

Usually, the stress increase in a local detail is considered to be proportional to the nominal stress. This allows the calculation of the hot-spot stress as a simple factor, called the stress concentration factor, K , times the nominal stress. Then the stress in the detail is given by

$$\sigma_{hs} = K \sigma_n. \quad (29)$$

In the current study, the chosen S-N curve has included the effects of local welding. Therefore, this section only focuses on finding the hot-spot (structural) stress.

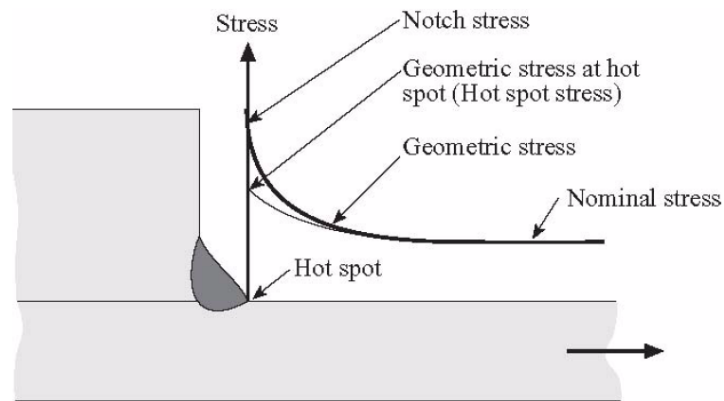


Figure 37. Illustration of the detail with the different stresses indicated. Image source: DNV Fatigue Note 30.7 DNV (2010a).

Class rules typically allow for using either tabulated values for the stress concentration factor or prescribe special procedures for calculating the factor using FE methods. Using Table A-2 case 3 (DNV (2010a)), the stress concentration factor (SCF) is found to be 1.27 for the considered detail.

Obviously, the values of SCF can significantly affect the fatigue life predictions. However, it is known that there are large uncertainties in the computation of SCF using the different methods suggested by classification societies, see, for example, Fricke (2002). Furthermore, as investigated by Li and Ringsberg (2011), for a local structural detail in the 4400TEU container ship, its stress concentration factor changes with time in a stationary sea state. This is due to different combinations of wave loads, horizontal bending, vertical bending and torsion etc., applied on the ship. To further investigate the uncertainty of fatigue life prediction caused by the SCF computations, three main methods suggested by DNV using FE methods are explained and compared in this chapter.

The geometry may be modelled either with shell elements or solid elements. For shell elements, 8-node elements are recommended but under certain restrictions also 4-node shell elements are allowed. The investigation in the following section will use the methods as described in DNV Fatigue Note 30.7.

For 4-node shell elements the stresses are extracted to the stiffener edge (up to the top edge in Figure 42) using second-order interpolation of the element averages. See also Figure 38 where the stress read-out procedure is illustrated. These stresses are then used to fit a second-order polynomial to extract the stresses at $t/2$ and $3t/2$ from the toe along the line A-A in Figure 38, in turn linearly interpolated to find the geometrical stress at the hot-spot. All shell elements used are square and of the same size in one model.

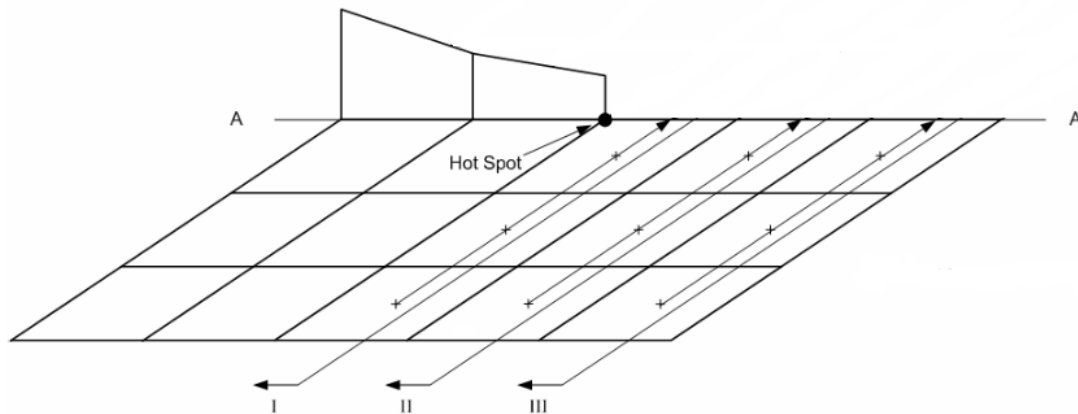


Figure 38. Methodology for stress extraction using 4- node shell elements. Image source DNV 2011.

The 8-node shell elements provide element edge surface stress points which are directly used for finding the stress read-outs at $t/2$ and $3t/2$ through linear interpolation. These two points are then linearly interpolated to find the geometrical stress at the hot-spot.

For the solid elements, 20-node hexagonal elements are used and the stresses are extrapolated by linear interpolation of the Gaussian points to the surface. These are then averaged to find the stress at the centre line from which the two stresses read-out points are found and interpolated to the hot-spot in the same manner as for the shell elements.

6.2 SCF computation using different methods

Firstly, the structural detail is modelled using 8-node square shell elements with the same element size as the thickness of the stiffener, 35mm. The expected stress increase prior to the extra material may be seen as well as the expected lower stress in the bracket until the stress field has evened out. The distribution of longitudinal stress around the considered detail is shown in Figure 39.

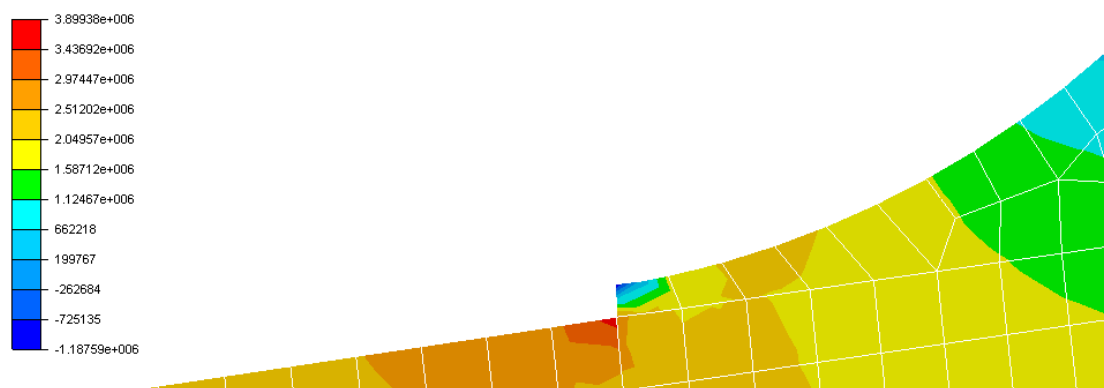


Figure 39. Longitudinal stress in the area around the detail.

To investigate the effect of element size and type on the SCF calculations, the structural details are modelled by 4-node shells, 8-node shells and 20-node

hexagonals, respectively. The element size ranges from $0.5t$ and t , where t is the thickness of the stiffener. This size range is chosen according to DNV class guidelines.

Figure 40 shows the result of these computations. A tendency towards larger stress concentration factors is seen for larger element sizes, despite the read-out points being the same for all sizes as described. It is also of interest to note that the 4-node shell elements provide the most consistent prediction under element size change.

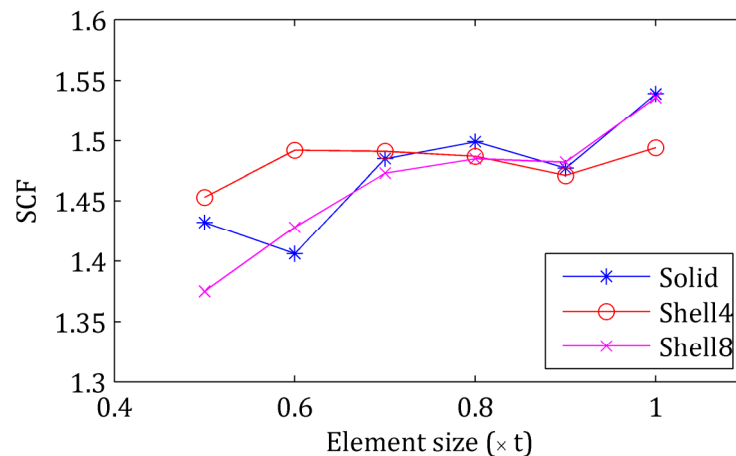


Figure 40. Stress concentration for a bracket stiffener weld on a stiffener without flange and a 25mm thick bracket as the element size changes for the three different methods.

6.3 Effects of SCF values due to local design

The stress concentration is caused by the discontinuity of local structures. It could be related to the geometrical change of the structure or the surrounding connections. In principle, the concentration is originated from the change of the local structural stiffness. Since cracks have been found in existing ships in the considered detail, it is of interest to study how the fatigue damage can be limited. Given an existing hull girder it would require very significant changes to decrease the global stress load. Hence, the remaining method available for reducing the fatigue damage is to refine the local structural details. It will lead to the decrease of the stress concentration factor (SCF). In the following, two ways of the local structural change are investigated. First, it is to investigate the effects of SCF due to the changes of thickness for the bracket which is connected to the beam. The other is to investigate the SCF variation due to introducing a flange in the I-shape beam.

6.3.1 SCF effects due to various bracket thickness

For the structural details in the current study, the bracket is welded with a simple beam, adding extra local stiffness. A stress increase is expected in the start of the bracket attachment. The amount of stress (SCF) increase depends on the ratio of bracket and beam stiffness. However, the SCF for such a detail provided by classes does not take the thickness of the bracket into account. To investigate the effect of the bracket thickness, the SCF for various bracket thicknesses is computed using 3 different element types, where the mesh size is chosen to be t or 35 mm.

A very clear dependence on the thickness or relative stiffness of the bracket and stiffener is shown in Figure 41. The SCF values for both shell models behave as expected. The values tend towards 1.0 for an infinitely thin bracket. It also indicates no stress concentration for the case of no geometrical variation. The result from the solid model does not behave similarly. This is because the weld is modelled in the solid case as a fixed height and linear slope, see Figure 43. The weld remains even though the bracket is removed. The presence of a slight slope of the weld at the hot-spot rather than the orthogonal corner also explains why the shell models produce larger stresses for thick brackets.

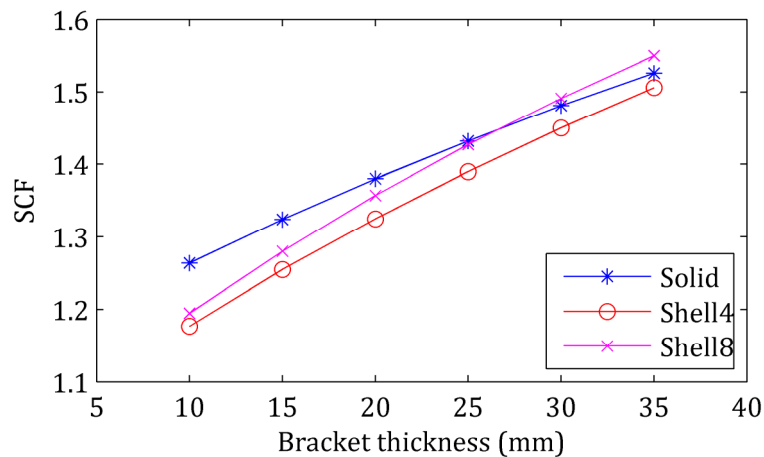


Figure 41. Stress concentration for a bracket stiffener weld for a stiffener without a flange and 35mm thick.

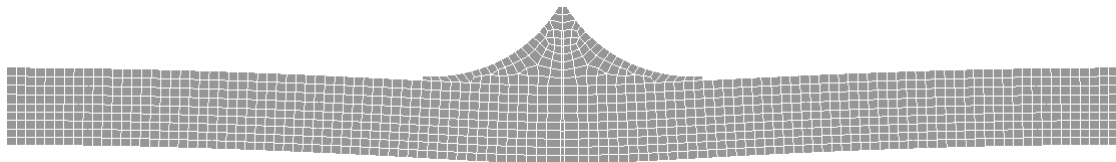


Figure 42. Mesh deformation of a model under longitudinal load. The mesh size here corresponds to the stiffener thickness. Note that the stiffener and bracket are here displayed upside down as compared to how they would be mounted in the ship.

All these calculations have been performed on the geometry seen in Figure 42, changing the mesh resolution for the different sizes. In one end of the stiffener, all degrees of freedom of the nodes have been clamped and in the other all except for the longitudinal are clamped and a longitudinal displacement is prescribed. Note, however, how the additional stiffness created by the symmetrical brackets leads to a vertical displacement of the beam.

This displacement may alter the stress distribution in the region surrounding the hot-spot. An additional set of calculations were therefore performed to investigate the effect of adding a deck plating of 60mm to the geometry in Figure 42. The deck plating adds significant extra bending stiffness and significantly reduces the vertical displacement seen in Figure 42, and, more correctly, models the surroundings of the detail in the ship.

Table 12 shows the result of the calculations for and element size of 35mm both with and without the plating present. Results indicate that a somewhat increased value of calculated stress concentration with the plating is present. This model is believed to more correctly represent the actual situation.

Table 12. Stress concentration factors for the detail modelled with and without deck plating. The bracket thickness used is 30mm and the element size equal to the element size.

Method	Without plating	With plating
Shell 4	1.45	1.51
Shell 8	1.49	1.55
Solid 20	1.48	1.56

6.3.2 Stress concentration with and without a flange

The geometry of the given bracket is already designed to limit the stress concentration significantly because of the large radius of the bracket and the small amount of initial additional material added. The fatigue resistance could be further improved using methods such as grinding to additionally even out the transition or shot peening in order to improve the material properties. However, limiting the investigation to geometrical changes this section investigates whether or not a stiffener of the corresponding stiffness but with a changed cross section may improve the fatigue life.

Now, the stiffener in the considered ship is a simple flat plate stiffener without a flange. However, many ships are designed using L-profile beams on the deck stiffeners. It could be of interest to investigate if there is any advantage or disadvantage of the two profiles with regard to stress concentration at the bracket connection.

This has been investigated by running an additional set of calculations now using an L profile for the stiffener but with the corresponding stiffness. The stiffness is kept the same to ensure that the effect seen above due to changes in relative stiffness is avoided. In order to obtain an equal cross sectional area the stiffener with a flange is taken as a 300x100x23/35 mm profile as compared to the original 300x35 mm one. These calculations were performed without the deck plating present.

Table 13 shows the results of these computations. Note that for the flange case the post-processing software does not allow for result extraction at the locations as required by the methodology for an 8-node shell element, which is why this result has been labelled as not applicable.

Here, the results from the shell model and the solid model predict different behaviours. Using the 4-node shell element a lower stress concentration is found when using the stiffener with a flange. This might be explained by the increased amount of material of the stiffener present close to the hot-spot, both the flange of 35mm and the waist of 23mm as compared to just a waist of 35mm in the non-flange case, resulting in a relatively locally less stiff bracket for the flange case.

In the computation with solid elements, a larger stress concentration factor is instead found. Note, however, that this is the maximum value from the two sides since the geometry is no longer symmetrical through the middle of the stiffener. To thoroughly understand the stress redistribution surrounding this asymmetrical case, seen in Figure 43, further study would be needed. For the extent of this investigation it is just noted that the flange risks introducing a locally larger stress concentration factor than the plate stiffener.

Table 13. Stress concentration factors for the detail for a stiffener with and without a flange. The thicknesses are altered to provide an equal relative stiffness of the bracket. Note that for the solid solution with a flange the SCF is asymmetrical, and the stated value is the mean of the two sides.

	Shell 4	Shell 8	Solid 20
No Flange	1.38	1.32	1.39
Flange	1.25	n.ap.	1.47*

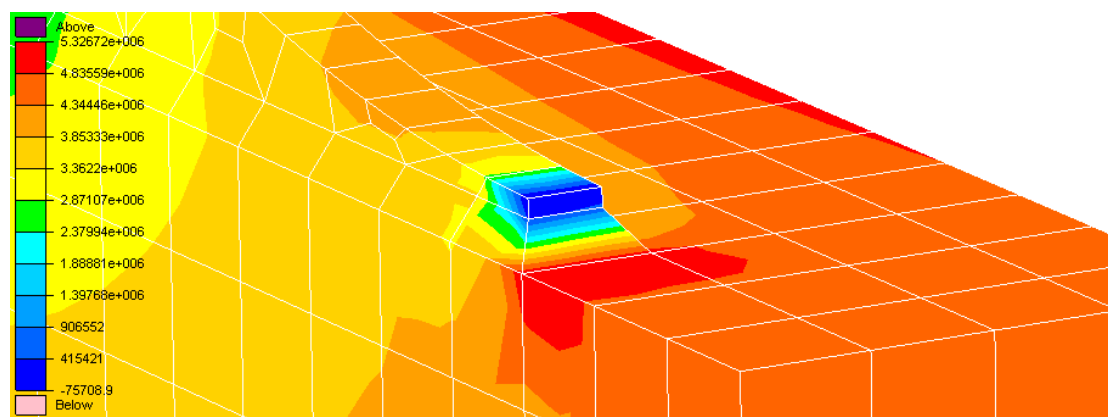


Figure 43. Stress concentration in solid mesh of a stiffener with flange.

6.4 SCF computation using the global ship FE model

As is indicated in Section 6.3, the stress concentration is related to the change of relative stiffness of the local structure. On the other hand, the relative structure stiffness also changes when different loadings apply on the structure. For the above computation, the structure is loaded by the pure longitudinal force in the stiffener. Also, according to DNV note 30.7 DNV (2010a), different loads such as horizontal and vertical bending can lead to different SCF values, although they cause almost the same longitudinal stresses in the stiffener. This section investigates the variation of stress concentration when the ship is loaded in real-sea environments.

A so-called sub-modelling approach is used for modelling the real stresses, DNV (2011d). The FE model is built for the entire ship structure with large shell and beam elements, referred to as the global model. Based on the solution of the global model, a

displacement field for all nodes in this model is computed. By choosing a sub-model of the local geometry with well-defined edges corresponding to element edges and nodes in the global model the calculated displacements may be used as boundary conditions for the local model to more accurately capture the local effects.

The sub-model is shown in Figure 44. The elements in the local structural detail are slowly refined to 21mm or $\sim 0.6t$ where t is the thickness of the stiffener. All quadrilateral elements used are 4-node shell elements and the local stress was found using the same methodology as previously described.

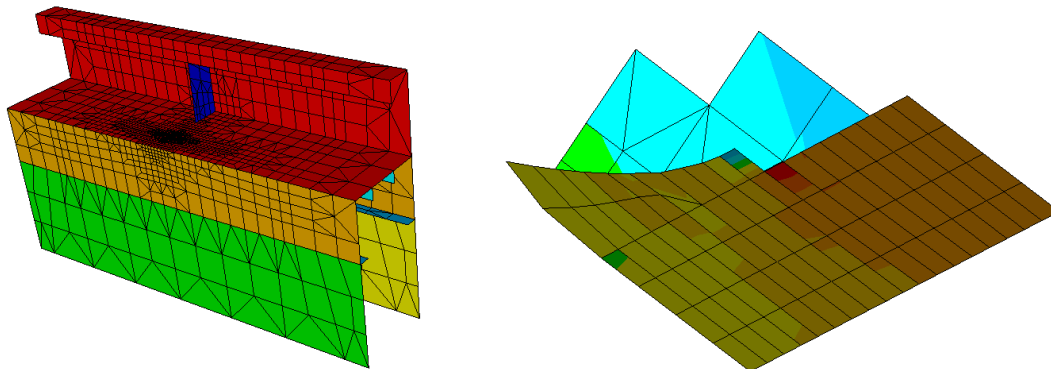


Figure 44. The entire sub-model to the left and a magnified view of the detail to the right. The shading in the left figure represents shell thickness and longitudinal stress in the right figure.

To investigate the stress concentration factor at the detail under different load scenarios, the global FE-model was subjected to horizontal and vertical bending separately, followed by an axial force and torsion. The global model was for these investigations clamped along the aft and displacements prescribed in the bulb to create the four load cases. Since the considered detail is in the mid-section of the ship it was assumed that any effects from the boundary conditions would be sufficiently small to be disregarded at the detail.

Table 14 shows the calculated stress concentration factors for the detail under the four different load cases. The global stress was here taken as the stress in the beam element present in the global model representing the stiffener in question.

The wide range in the calculated stress concentration factor for torsion is explained by the large longitudinal variation in normal stress in the beam elements along the ship. Between two subsequent bulkheads there is a large variation in stress due to torsion, and the relatively long constant stress elements used in the global model cannot accurately capture this, leading to a poor prediction of the global nominal stress.

The stress concentrations are considerably greater than both tabulated values and values found through only local FE-modelling in the previous section. The great difference is unexpected, but may partly be explained by the presence of the web further restricting the vertical deflection of the stiffener.

Table 14. Stress concentration factors as calculated by a displacement-driven FE-sub model under four different loads.

Applied load	SCF
Longitudinal	1.89
Horizontal bending	1.94
Vertical bending	1.87
Torsion	1.64-2.62

One additional difference is that the global stress compared for these values is the stress in the beam element from the global model. These elements have constant stress formulations and therefore do not allow for extraction of the global stress at the precise longitudinal position of the detail.

To further investigate the stress concentration factor of the detail in the ship a time domain simulation of the ship with a heading angle of 125 and a significant wave height of 6m was run. A series of global stress σ_g found from the global beam element, the local stress found using the methodology described above and the nominal stress σ_n were extracted. The nominal stress was here found as the mean stress of all elements in a cross section of the stiffener 0.5m from the bracket connection in the sub- model.

These extracted stress values were used for constructing a two- time series of stress concentrations shown in Figure 45. These take the mean values of 1.80 and 1.74, respectively.

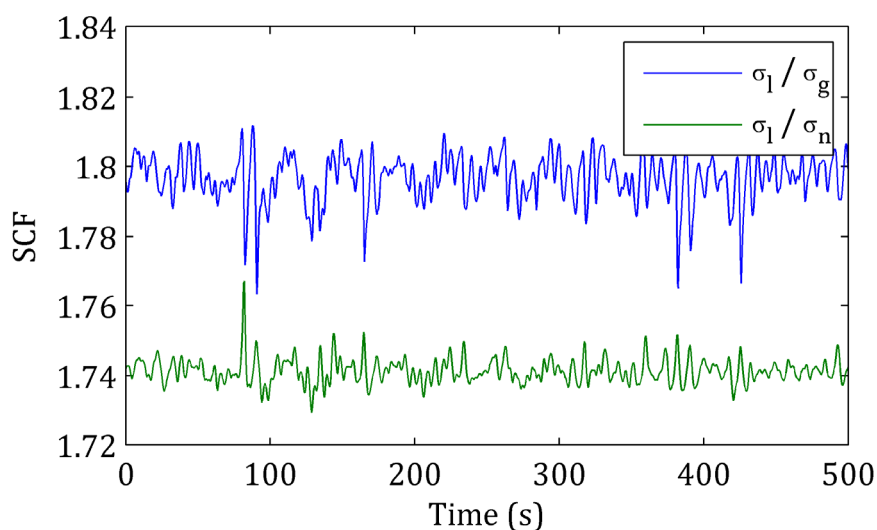


Figure 45. Stress concentration factor over time using nominal stress from the global model beam elements and stiffener mean, respectively.

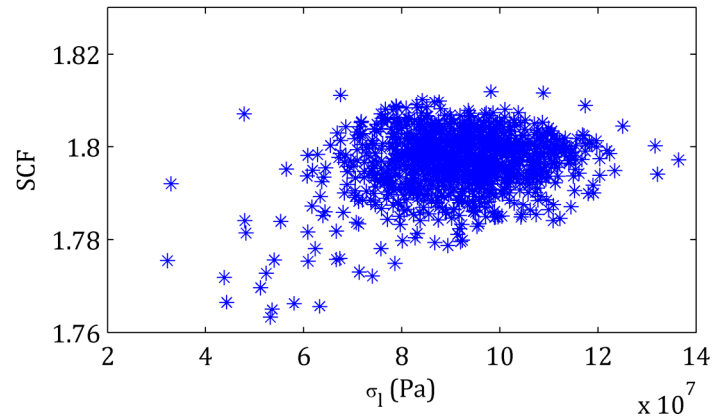


Figure 46. An illustration of the correlation between the local stress magnitude and stress concentration factor (global) in a time series.

Figure 46 shows the global stress concentration factor plotted against the local stress value. As expected, there is none or very weak correlation between stress level and factor. However, referring back to Figure 45, there is some indication on a pattern for when there is a change in the effective SCF. To investigate this further the correlation between sectional forces and the SCF using σ_g is shown in Table 15.

Note the significant correlation between torsion and the calculated stress concentration, also illustrated in Figure 47. It shows the correlation between torsion and the SCF calculated using σ_n . There is a significantly stronger correlation when using the stress from the global beam element. This agrees with the greater variation found in Figure 45 for the beam stress. This variation partly contributes to the inability of the constant stress beam elements to capture the stress distribution in the presence of the steeper stress slopes between bulkheads under torsion.

Table 15 The correlation between different sectional moments and the stress concentration factor found using σ_g .

Section moment	Correlation
Torsion	-0.68
Horizontal bending	0.15
Vertical bending	-0.41

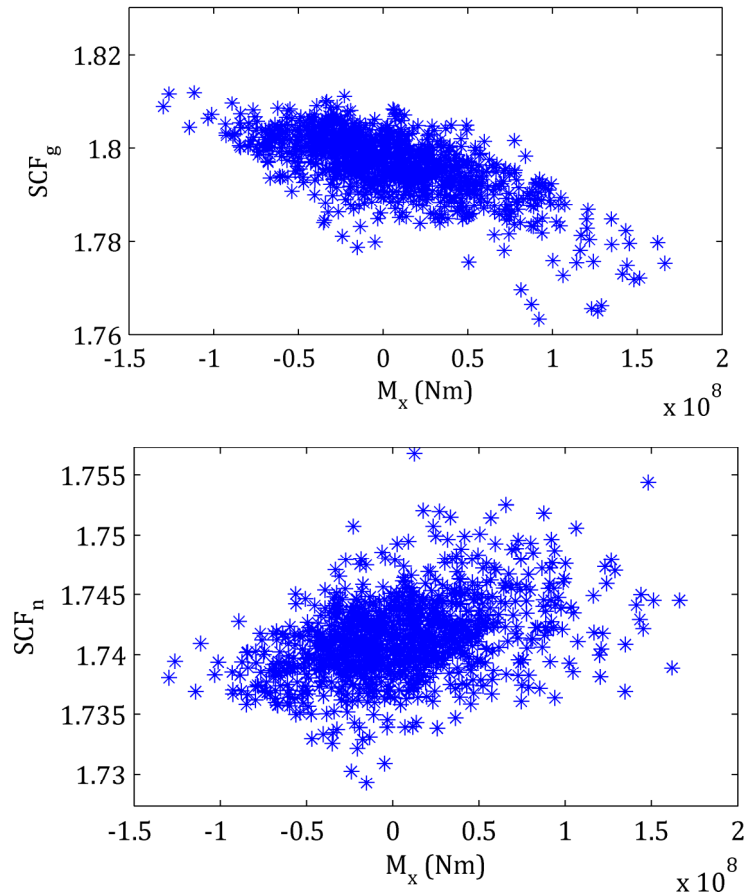


Figure 47. Illustrations of correlation between torsional section force and stress concentration calculated using global stress σ_g (top) and nominal stress σ_n (bottom) as described in the test.

6.5 Concluding remarks

The differences in computed stress concentration may seem small, but by including the effect of the exponent in the S-N curve the resulting change in calculated fatigue damage may be substantial. The author finds it curious that the factors found in the tables provided by class do not take the relative stiffness of the stiffener and bracket into account. A possible explanation may be that bracket thicknesses are commonly similar, and, based on the result in Figure 41, a bracket thickness between about 15 and 20 mm would lead to a value well matching the tabulated value. Nevertheless, this result clearly indicates the advantage with regard to local stress concentration of using as thin brackets as possible - at a critical location it may be appropriate to reduce the thickness significantly and instead use stiffeners on the bracket to prevent buckling.

The difference between the three methods for calculating SCF's using FE models produce slightly different results. The conservative option based on the results found here would be to use the solid elements or 8-node shell elements. However, no attempt to verify against experimental data has been performed.

More interesting is the significantly increased stress concentration factor found when using the sub-modelling approach of the local geometry under the displacement field from the girder deformation. It is noted that there appears to be little difference between the SCF under horizontal, vertical and torsional bending of the ship girder. This is to be expected since the stiffener and considered detail is almost exclusively subjected to longitudinal stresses. However, the great increase in stress concentration as compared to the results found by modelling just the stiffener or the tabulated value is surprising. It may be explained by additional local deformations creating stresses - the web frame may, for example, further prevent vertical deformation of the stiffener and thus increase the SCF. The results do indicate that for the considered detail the tabulated factor of 1.27 is not sufficiently conservative. It is therefore recommended that a model of the surrounding geometry is used for calculating a correct concentration factor for a ship detail even under uniaxial load.

Finally, it is found that under sea loads the stress concentration factor is effectively constant over time, and that a fixed stress concentration factor is indeed a good model for translating global girder forces to local stresses.

7 Fatigue assessment and analysis

Using the methods described and investigated in the preceding chapters, the stress history in the considered detail can now be calculated. This section will use these stress histories to compare and evaluate the fatigue damage using different combinations of the methods previously described. In addition, several spectral fatigue compensation models are tested and compared to the fatigue as calculated from direct rain-flow counting and the narrowband approximation.

Now, if the time series of structural stresses are available, the corresponding fatigue damage can be estimated by the rainflow counting (RFC) method. The rainflow method is considered to give us an accurate estimation of fatigue damage. For ship fatigue assessment, structural stresses are often assumed to be Gaussian-distributed and uniquely defined by a spectrum. Therefore, it is convenient to estimate the fatigue damage by a spectral method. Most of the current spectral methods are based on the so-called narrowband approximation (NBA) to approximate the RFC damage. Various correction procedures are introduced to decrease the overestimation from NBA, such as the method introduced by Benasciutti and Tovo (2007) (denoted by BT), Zhao and Baker (1992) (denoted by AB), the Wirsching-Light correction, Wirsching and Light (1980) (denoted by WL), the Dirlik method in Dirlik (1985) (denoted by DL) and the method from Lutes and Larsen (1990) (denoted by LL), respectively.

In order to investigate the discrepancy of different spectral methods from the RFC method for ship fatigue assessment, the structural stresses were computed using non-linear hydrodynamic analysis followed by the engineering beam theory for various sea states. It is found that for sea states with significant wave heights from 0.5 to 8.5 m, ship response appears very close to Gaussian with $E[\gamma_1]=0.044$ and $E[\gamma_2]=0.009$ for skewness and excess kurtosis and skewness, respectively. Furthermore, fatigue damages computed by some spectral methods, NBA, DL and LL, are compared with the RFC method in Figure 48.

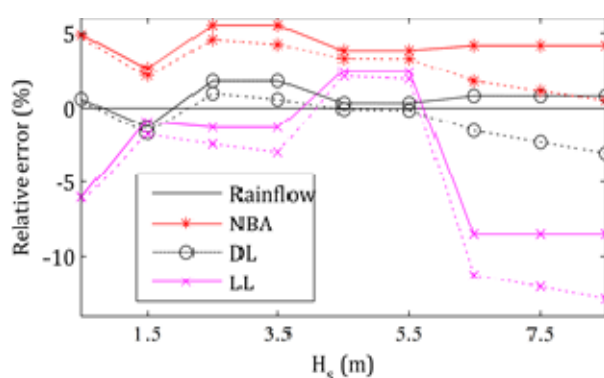


Figure 48. The relative error in damage prediction for some spectral methods as compared to direct rain-flow counting. The dotted lines indicate the use of the non-linear solver, while solid lines are from the linear solver.

Note that the Lutes-Larsen method, the only one to depend on only one moment, clearly performs the worst out of the correction methods. Also, the Dirlik method

sometimes provides an under-prediction. In fact, only the narrowband approximation itself provides a constantly conservative prediction. The damage predicted by the NBA is close to the value obtained by direct rain-flow counting, in this case within 5%.

In order to find the most efficient way for a direct ship fatigue assessment, both the computation power and accuracy of different estimation procedures are compared in Table 5. The time is measured on an iCore5 workstation with 8 GB of RAM. The table presents results from four main types of calculations:

- Panel method in sea state combined with a global FE solution,
- Panel method in sea state with stresses calculated using the engineering beam theory,
- Panel method to create RAOs combined with the engineering beam theory
- Strip theory with the engineering beam theory.

Table 16. A comparison of the calculated damage rate normalized against that for rain-flow counting and the approximate required computer time for a simulation of an additional sea state on a low end desktop computer. All simulations using the engineering beam theory are calculated from 9 simulations with H_s ranging from 0.5 to 8.5 m in increments of 1m and evaluating damage from both the port and the starboard side. The simulations using the FE for structural stresses are only evaluated in one sea state.

Method	Ty	$E[D^*]$	$Var[D^*]$	First calculation	Additional calculation
Non.P.+FEA+Rfc	1	<0.5	-	18 h	18 h
Lin.P.+FEA+Rfc	1	<0.5	-	15.5 h	15.5 h
Non.P.+EBT+Rfc	2	1.157	0.032	6 h	6 h
Lin.P.+EBT+Rfc	2	1.000	-	3 h	3 h
Lin.P.+EBT+NBA	2	1.036	0.014	3 h	3 h
Non.P.+EBT+NBA	2	1.187	0.029	6 h	6 h
Lin.P.+EBT+BT	2	0.980	0.013	3 h	3 h
Lin.P.+EBT+LL	2	0.984	0.014	3 h	3 h
Lin.P.+EBT+ZB	2	0.931	0.016	3 h	3 h
Lin.P.+EBT+WL	2	0.873	0.013	3 h	3 h
Lin.P.+EBT+DL	2	0.999	0.014	3 h	3 h
Lin.P.+EBT+LL	2	0.958	0.052	3 h	3 h
Freq.P.+EBT+NBA	3	1.057	0.134	49 h	60 s
Freq.P.+EBT+BT	3	0.998	0.127	49 h	60 s
Freq.P.+EBT+ZB	3	1.005	0.128	49 h	60 s
Freq.P.+EBT+DL	3	1.022	0.130	49 h	60 s
Strip+EBT+NBA	4	1.273	0.193	60 s	60 s
Strip+EBT+BT	4	1.168	0.178	60 s	60 s
Strip+EBT+ZB	4	1.170	0.180	60 s	60 s
Strip+EBT+DL	4	1.142	0.174	60 s	60 s

In the table, the abbreviations “Non” and “Lin” refer to non-linear and linear hydrodynamic analysis, respectively; “P” denotes the panel method; “FEA” and “EBT” denote finite element analysis and the engineering beam theory, respectively. All results are presented normalized against the fatigue damages calculated by using the linear panel method in combination with the engineering beam theory and rain-flow counting.

Comparing the damage prediction with loads from time domain hydrodynamic simulations using panel methods and frequency domain results constructed by combination of RAOs show that the average prediction over all sea states is very good. However, there is an over-prediction for lower wave heights and under-prediction for higher wave heights. Consequently, for damage from a long-term sea state the frequency domain results would probably predict greater fatigue damages, since the smaller wave heights are comparatively more common.

The damage predicted by the strip theory method is generally higher than the corresponding damage from the panel method, especially for the sea states with lower wave heights. No attempt has been made to decrease this difference. Table 5 also shows the approximated time required for using the method in question. The great difference between especially frequency domain computations and a full hydrodynamic and FE solution provides a clear motivation for its general use.

7.1 Concluding remarks

The fatigue damage prediction using hydrodynamic loads from strip theory, frequency and time domain panel methods and structural stresses from the FE and engineering beam theory analyses have been compared for a fully laden container ship in bow seas.

It is found that when considering a specific structural detail unaffected by local plate buckling due to water pressure in the mid-section and ignoring vibrational responses, the narrow-band approximation provides a good enough measure of the rain-flow damage. This is shown by examples for both linear and non-linear panel method solvers combined with the engineering beam theory. It is concluded that a frequency domain analysis of fatigue damage for the same detail is a time-saving alternative with an expected error of less than 6% compared to the damage from a linear time domain analysis. However, accounting for non-linear effects in the hydrodynamic load calculation creates noticeable differences in heavy seas.

8 Conclusions and proposed methodology

This section will present and discuss some of the conclusions drawn in previous chapters as well as present the proposed methodology for fatigue assessment in the considered detail. First, the main conclusions from the thesis are presented together with some discussions, to be followed by a summary of the proposed methodology and finally some comments on recommended further work.

It is very interesting to note that there were several problems with Wasim, the hydrodynamic panel solver used, with regard to fatigue estimation. In addition to the rather severe convergence problems encountered there were issues with sectional moments and noise in the output. The noise manifests as one sample long peaks in calculated moments, often of magnitude 10% above that of the cycle amplitude. This noise may be removed by using a low pass filter, but nevertheless provided a severe fatigue over-estimation of up to 45% if not handled properly. Discussions and studied reports indicate that this is not always done when using this solver, indicating that the results may not be reliable.

In addition, the solver does not account for the forces from the soft-spring system when calculating sectional forces, leading to presented moments that are significantly different from the forces actually present in the simulated ship. It may be discussed which measure is the most correct since no spring system exists on the real ship. Regardless, this creates a large deviation between FE solutions and stresses calculated from beam theory using the sectional moments.

Not enough comparisons have been made to judge if strip theory is sufficient for the present case or if the more time-consuming panel method should be used for the construction of response amplitude operators. It is, however, found that the difference between using the linear and non-linear solver is sufficiently small for the investigated ship to motivate usage of the linear method. This may indicate that also strip theory could prove to be sufficient.

Two methods have been used for calculating the global girder stresses, engineering beam theory and a coarse FE model of the main structural members. The results clearly show that for details with primarily longitudinal stress and under horizontal and vertical bending of the hull girder the beam theory approach is sufficient. It is further shown by decomposition into contributions from warping and bending that the beam theory approach is sufficient provided that correct measures on the warping properties are available.

To investigate the importance of the three contributions the ship was simulated in several sea states and the resulting stress in the detail was decomposed into the stress created by vertical bending, horizontal bending and warping, respectively. The results indicate that for the considered detail in the mid-section the contributions from warping and horizontal bending interfere destructively and are of similar magnitude. This means that approximating the stress by just the vertical bending contribution provides a relatively good measure on the total stress with an error of no more than 30%. However, if either warping or horizontal bending is included both effects must be accounted for; otherwise the errors are shown to be as large as 80%.

However, a detail in a cross section just forward of the engine bulkhead is also considered. The results from this detail show that the warping component is increasingly more important and an approximation using just vertical bending is no longer sufficient.

Having obtained the corresponding nominal stress at the location of interest, the stress concentration due to local geometry was next investigated. Three methods based on FE analysis as recommended by the considered classification society were tried and the calculated concentration factors from the three methods were similar. In particular, it was noted that using the provided methodologies the calculated stress concentration factor was only marginally affected by the element size chosen. However, as expected, the relative stiffness of the bracket to the stiffener has significant effect on the stress concentration and it is somewhat surprising that the tabulated values in the class rules do not allow for variations here.

Additionally, the stress concentration factor was calculated in the global hull FE model using a sub-modelling approach. The stress concentrations factors found using this method are larger than the previously obtained values, but remain similar under different loading conditions on the hull girder. It is interesting that this method provides larger values than those tabulated in classification rules, indicating either an error in procedure or that the tabulated values may not be conservative for all cases.

Finally, the rainflow fatigue damage given the load history is approximated by several spectral methods. It is concluded that even the simplest spectral method, the narrowband approximation, provides a very good measure of the rainflow method. The error is significantly smaller than those from previous calculation steps. In addition, the method has mathematically previously been shown to always provide conservative values.

However, given additional vibrational responses or otherwise bi-modal responses may invalidate this and lead to large over-prediction from using the narrowband approximation, requiring application of one of the spectral compensation methods.

8.1 Proposed methodology

For assessment of fatigue damage accumulation in a ship detail under uniaxial longitudinal load and unaffected by local pressures it is recommended that the hydrodynamic loads are calculated using RAOs constructed for the particular ship, the heading angle and ship speed using a linear panel method. When constructing the response amplitude operators for sectional bending moments it is important that phases are correctly accounted for and that if unwanted noise is present in the signals an appropriate filter is applied. The longitudinal stress in the detail should be constructed by combining the contributions from either just vertical bending or vertical, horizontal and torsional contributions.

However, if the detail is expected to be subjected to significant contributions from warping, or, if a sufficiently accurate model for warping properties is not available, a direct calculation approach using a linear panel method and global FE model of the hull girder is to be used. Alternatively, the stress regression method presented may be sufficient in this case.

To account for local stress concentrations the recommended approach is to calculate the stress concentrations in the hull using an FE sub-modelling approach to fully account for all local deformations. However, if a hull girder model is not available, local shell models of the detail or tabulated values are likely to provide sufficient measures.

Finally, for fatigue evaluation the narrowband approximation is sufficiently accurate to approximate the rain-flow counting result and there is no need to use any compensation methods or to use direct rain-flow counting when disregarding vibratory responses.

8.2 Further work

The major limitation of this work is that only one particular detail has been studied on one particular ship. It is therefore recommended that many further examples are investigated in order to verify the conclusions drawn here.

Additionally, several simplifications have been assumed, such as not accounting for residual stresses or corrosion and the usage of one-slope S-N curves only. Since these effects are commonly accounted for when making fatigue life estimations in industry their effects on the presented result should also be investigated.

Of particular interest is how well the engineering beam theory assumption works for calculating the longitudinal stresses in the hull girder, provided there are correct cross sectional moments. However, as explained above, the major difficulty is the approximation of the warping contribution - the torsion moments are readily computable using, for example, panel methods but the bi-moment or the torsional rigidity of the particular location is difficult. It would be of interest to study several ships to try and find empirical or semi-theoretical equations describing this as a function of the longitudinal position to allow for accurate accounting for warping without using FE calculations. This should be combined with a further study of the regression of stresses, since additional experiments by the author indicate very good agreement when using the correct sectional moments.

9 References

- Benasciutti, D. and Toivu, R. On fatigue damage assessment in bimodal random processes. *Int. J. Fatigue* (2007) **29**:232-244.
- Brodtkorb, P.A., Johannesson, P., Lindgren, G., Rychlik, I., Ryden, J., "WAFO – a Matlab toolbox for analysis of random waves and loads", *Proc. 10th Int. Offshore and Polar Engng Conf.* Seattle, USA, Vol III, pp. 343-350
- Dirlik, T. Application of computers in fatigue analysis. PhD thesis, University of Warwick, Warwick, U.K., 1985
- Ditlevsen, O. Stochastic wave loads on tubular offshore structures, models for dynamics and reliability analysis, Lecture notes for offshore structures course, 2nd edition. Technical University of Denmark, Copenhagen, Denmark 2002.
- DNV [Det Norske Veritas]. *Classification Note 30.7*. Høvik, Norway 2010a.
- DNV [Det Norske Veritas]. Sesam 2011 DVD Release, Release Notes, Høvik, Norway 2011b
- DNV [Det Norske Veritas]. Sesam User Manual, Høvik, Norway 2011c
- DNV [Det Norske Veritas]. Sestra User Manual, Høvik, Norway 2011d
- DNV [Det Norske Veritas]. *Strength analysis of hull structures in container ships*, Høvik, Norway, 2011e
- DNV [Det Norske Veritas]. Wasim User Manual, Høvik, Norway 2011f
- Doerk, O., Fricke, W. and Weissenborn, C. Comparison of different calculation methods for structural stresses at welded joints. *Int. J. Fatigue* (2003) **25**:359-369.
- Fricke, W., Cui, W., Kierkegaard, H., Kihl, D., Koval, M., Mikkola, T.,... Yoon, J.-H. (2002). Comparative fatigue strength assessment of a structural detail in a containership using various approaches of classification societies. *Marine Structures*, 1-13.
- Janson, C-E (Editor), *Waves, Motions and Manoeuvring (Lecture Notes)*, Gothenburg, Sweden, 2012
- Lewis, E.V. (Editor) *Principles of Naval Architecture 2nd edition Volume 3 Motions in Waves and Controllability*, The Society of Naval Architects and Marine Engineers, Jersey City, 1989
- Lutes, L.D. and Larsen, C.E. Improved spectral method for variable fatigue prediction, *J. Struct. Engng* (1990) **116**:1149-1164.
- Mao, W. Fatigue assessment and response prediction of ship structures. PhD thesis, Chalmers University of Technology, Gothenburg, Sweden, 2010

- Nautical Institute. (January 2007). Time to wake up to the consequences of fatigue. *Alert! The International Maritime Human Element Bulletin*, No 13.
- Rychlik, I. On the narrow-band approximation for expected fatigue damage. *Engng Mech.* (1993) **8**:1.4.
- Smith, R. (1990). The Versailles railway accident of 1842 and the first research into metal fatigue. *Fatigue 90 vol. IV* (ss. 2033-41). Birmingham: Materials and Component Engineering Publications.
- Stephens, R. I. (2001). *Metal fatigue in engineering*. John Wiley & Sons.
- Storhaug, G., Moe, E. and Holtsmark G. Measurement of wave-induced vibration and fatigue loading onboard two container vessels operating in harsh environment. *J. Offshore Mech. Arct. Engng* (2007) **129**:279:289.
- Storhaug, G., Moe, E. Measurements of wave induced vibrations onboard a large container vessel operating in harsh environment. *DNV [Det Norske Veritas]*, Høvik, Norway
- Suresh, S. *Fatigue of materials*. Cambridge University Press, 1991.
- Thelandersson, S. Analysis of thin-walled elastic beams. Lund Institute of Technology, Lund, Sweden, 1987.
- Zhao, W. and Baker, M.J. On the probability density function of rainflow stresses range for Stationary Gaussian processes. *Int. J. Fatigue* (1992) **14**:121-135
- Li Z., Direct Calculation of Wave-Induced Loads and Fatigue Damage of Container Vessels, Licentiate thesis, Chalmers University of Technology, Gothenburg, Sweden, 2011
- Li, Z., Ringsberg, J.W. Direct calculation of fatigue damage of ship structure details. In *Proceedings of the ASME 2011 30th International Conference on Ocean, Offshore and Arctic Engineering (OMAE2011)*, Rotterdam, the Netherlands, 2011.
- Li, Z., Ringsberg, J.W. Fatigue routing of container ships – assessment of contributions to fatigue damage from wave-induced torsion and horizontal and vertical bending. *Ships Offshore Struct.* (2011) **7**:119-131
- Wirsching, P.H. and Light, C.L. Fatigue under wide band random stresses. *J. Struct. Engng* (1980) **106**:1593-1607

Appendix A – Cross sectional properties

This appendix introduces additional measures made on the FE model to find moments of inertia, etc., that correspond to the modelled geometry.

This first part describes one way of approximating the cross sectional properties of the mid-section of the FE model. By cutting out the mid-hold including bulkheads and repeating it, a long slender beam is created. Applying forces and boundary conditions to this beam allows for a comparison to the expected displacements calculated using the beam equation and calibrating the cross sectional properties to attain matching deformations.

The beam model used in all calculations is elongated to be 479 m long and may be seen in Figure 49. This length is deemed long enough to expect the beam equation to produce good predictions.

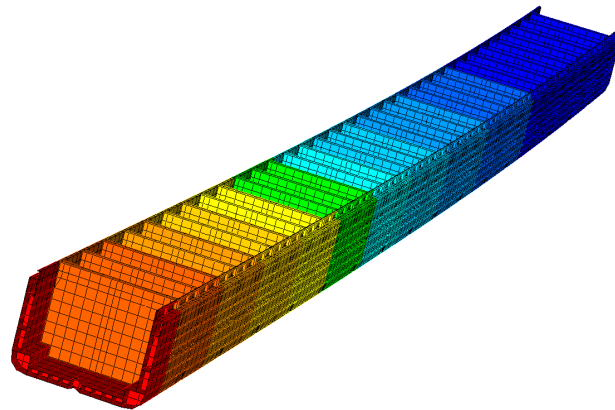


Figure 49. A view of a deflected FE-model of the elongated mid-section. Shading represents vertical displacement of the corresponding element.

To allow for a comparison between the deformation of the FE model a reference is needed. For slender beams and a small lateral deflection the beam equation is a fourth-order differential equation given by

$$\frac{d^2}{dx^2} \left(EI \frac{d^2 w(x)}{dx^2} \right) = 0 \quad (30)$$

where w denotes the deflection of the beam at the location x and E, I are the elasticity module of the material and area moment of inertia of the cross section, respectively. To determine the shape of the expected displacement, boundary conditions are applied and the ODE solved for. In the vertical case, the beam has been clamped in one end and a vertical force applied in the other, leading to the expected deformation

$$w(x) = \frac{P}{6EI} (2l^3 - 3l^2 x + x^3), \quad (31)$$

where l denotes the length of the beam and P is the applied force. For horizontal bending a force is not as simple to apply since the exact shear centre is unknown and will be located outside the cross section. This would lead to additional torsion of the beam if simple nodal forces were applied at the end.

Instead, consider a beam clamped in one end, and in the other clamped in all but on the translational direction where a force is applied. First, solving the beam equation ODE by integration leads to

$$w(x) = \frac{ax^3}{6EI} + \frac{bx^2}{2EI} + cx + d . \quad (32)$$

Now, applying the boundary conditions for the clamped end

$$\begin{cases} w(0) = 0 & \Rightarrow d = 0 \\ w'(0) = 0 & \Rightarrow c = 0 \end{cases} , \quad (33)$$

and at the other end we know the shear force and that the angle is zeros since these degrees of freedom were clamped, thus

$$\begin{cases} w'(l) = 0 \\ w'''(l) = -\frac{F}{EI} \end{cases} . \quad (34)$$

Solving this equation system yields

$$w(x) = \frac{Fx^2}{2EI} \left(\frac{l}{2} - \frac{x}{3} \right) . \quad (35)$$

To calculate the cross sectional area a simple compressive force was applied to the ship beam and using Hooke's law to solve for the area. Figure 50 shows the deformations for vertical and horizontal bending as predicted by the beam theory and as measured from the FE model with the fitted cross sectional properties. Note that these values were chosen so as to minimize the root mean square of the distance between the two curves. Table 7 shows the values of the cross sectional properties as fitted.

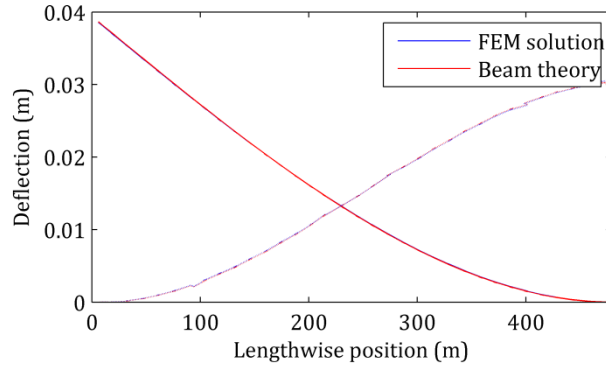


Figure 50. The deflection of the ship-beam as a function of location under both horizontal and vertical bending with calibrated cross sectional properties. Note that it is almost impossible to distinguish the theoretical prediction and measured values.

Stress distribution in section

Using the same elongated mid-section beam as in the previous section, this section introduces an additional measure on the cross sectional properties. Using the same boundary conditions as previously for horizontal bending, i.e. one end clamped and the other end clamped in all but one shear direction, the same deformation is expected, given by

$$w(x) = \frac{Fx^2}{2EI} \left(\frac{l}{2} - \frac{x}{3} \right). \quad (36)$$

Now, the shear force will be constant and equal to the applied shear force throughout the beam. Using the second derivative of the deflection, the bending moment at a position x in the beam due to the load is given by

$$M(x) = -EI \frac{d^2w}{dx^2}, \quad (37)$$

or for the present case

$$M(x) = F(x - l/2). \quad (38)$$

Now, using the engineering beam theory the longitudinal stress for a position in the cross section is a function of the bending moment and given by

$$\sigma_n^i = \frac{M_i}{I_i} x_i. \quad (39)$$

where x_i is the orthogonal distance from the neutral axis and I_i is the corresponding area moment of inertia. Furthermore, when the beam undergoes pure bending all normal forces are expected to be a consequence of this bending. Using the derived equation for the bending moment in the beam it is concluded that in the middle of the beam no normal stresses are expected. Thus, to be able to study the distribution, a location about a quarter from the end of the beam is chosen, so as to limit any effects

of the boundary and still obtain a large cross sectional moment. For the remainder of this investigation a lengthwise position in the beam of 120.7 m from the end is chosen, leading to an expected bending moment of $M \approx -18046200$ in this section given the applied shear force of 0.15 MN. Figure 51 illustrates the deformation and stress distribution in the beam for these two cases.

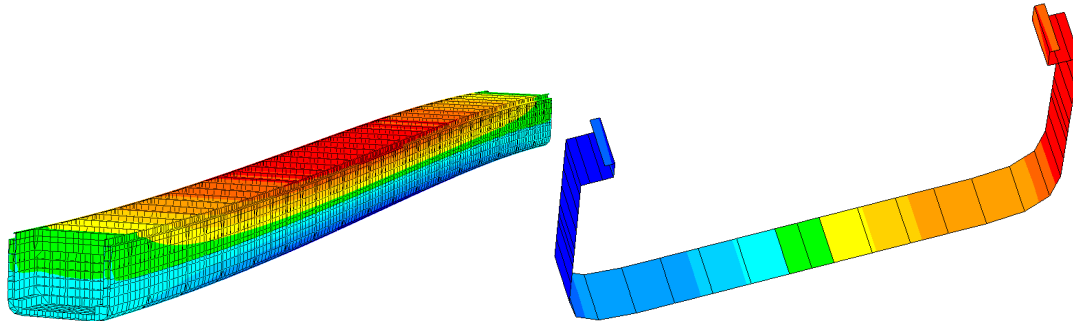


Figure 51. Longitudinal stresses in entire beam under vertical deflection to the left and in shells of one section under horizontal bending to the right. The blue shades represent negative stress and red positive stress.

Figure 52 shows the normal stress magnitude and location in the cross section for elements under both horizontal and vertical bending. It is concluded that based on the area moment of inertia calculated for the beam, the engineering beam theory constantly over-predicts the magnitude of the stresses compared to the FE model for horizontal bending, with especially great deviations for large y values and high up in the structure. The two obvious outliers marked with crosses are the two top plates seen in Figure 52.

Instead, fitting a line in the least square sense to the data in the figure leads to a calculated value of $I_h' = 767$. Note, however, that the initial line presented in the figure better fits the data in the range $(-10, 10)$, whereas the fitted line will be significantly affected by the large group of points out by the sides. The same deviation is not seen for vertical bending where the fitted line well matches the previous value, apart from three data points representing the hold coamings. This is explained by the fact that they are not being continuous throughout the length of the beam.

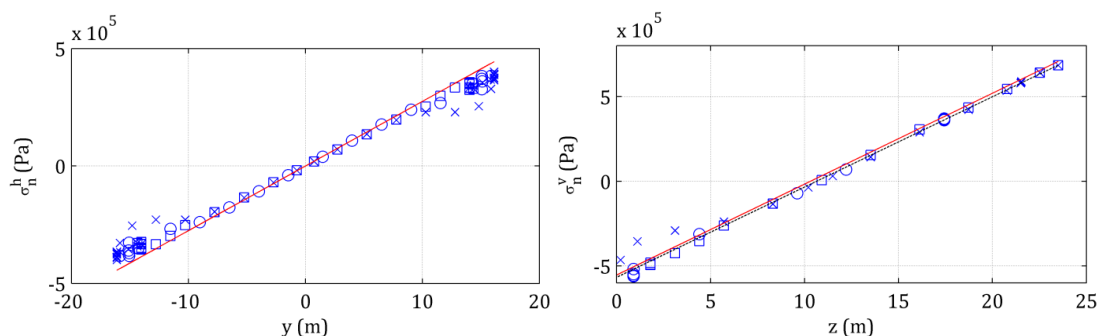


Figure 52. Longitudinal stress in elements of the cross section marked with markers. The squares represent data from inner plating, crosses from outer plating and circles for girder elements. The red line shows the predicted values using the engineering beam theory and the blue a least square fit to the data points. Data for horizontal bending are shown at left and vertical bending at right.

To investigate the position of the neutral axis it is first to be noted in Figure 51 that, as expected, the neutral axis seems to have a constant vertical position throughout the length of the ship. To investigate this in more detail, 14 half-sections of the outer plating were extracted along half the length of the beam (since it is symmetrical). Sections closest to the end and the mid-section were excluded since they are expected to give less reliable results due to the presence of boundary conditions and low stresses, respectively. Plotting the longitudinal stress as a function of the vertical position for each of the sections individually and fitting straight lines in the least squares sense results in Figure 53. The different slopes are explained by the difference in bending moment along the beam predicted by Eq. (38). Intersection of the lines yields a neutral axis of 10.75.

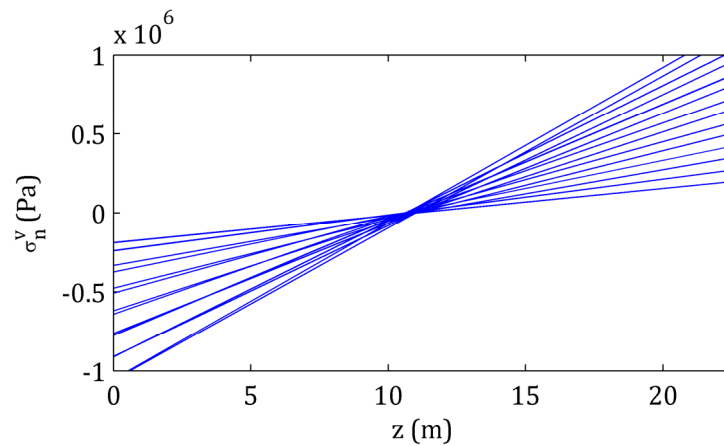


Figure 53. Longitudinal stress in different cross sections as a function of the vertical position.

Under pure axial loading, the engineering beam theory predicts that the normal stresses should be uniformly distributed - the result of subjecting the beam to pure axial loading with a compressive force of $F = 760\,000$ results in Figure 54.

The distribution is not uniform as expected. Rather, the bottom is subjected to relatively higher stresses than expected and the side plates lower. All resulting values found in this section are listed in Table 7.

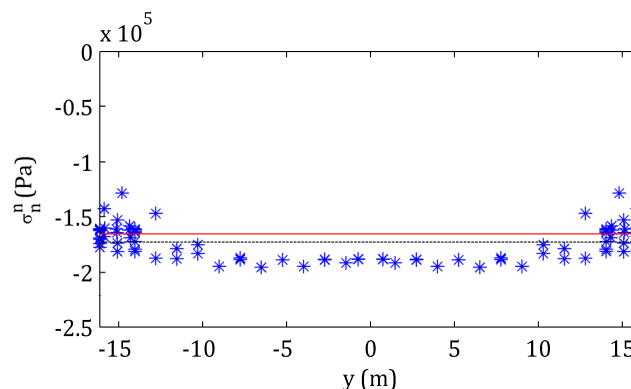


Figure 54. The distribution of normal stresses due to axial loading through the cross section. The upper red line shows the expected uniform distribution from the deformation-calculated cross sectional area and the lower black line the mean value of the stress in the plates.

Appendix B – Stability in hydrodynamic solver

This appendix includes some additional investigations made into the stability of the panel method solver used for the hydrodynamic calculations.

Calm water calculations

A calm water calculation was made using the configuration described. Running this simulation and plotting the corresponding motion of the ship results in Figure 55.

As may be seen from this graph, the initial position is not a stable equilibrium of the ship. However, after 1,000s the ship has converged to a stable position, described by the data in Table 17. Now, the panel solver allows configuration of the initial position of the ship. Using the equilibrium position just calculated and running a new calm sea calculation only changes the initial position results in no further change, indicating that this initial position is stable and was therefore subsequently used as an initial condition.

Table 17 *The difference in position between the initial configuration and stable equilibrium of a ship in calm sea.*

Surge	Sway	Heave	Roll	Pitch	Yaw
0.341 m	0.0	-0.005 m	0.0	0.019 deg	0.0

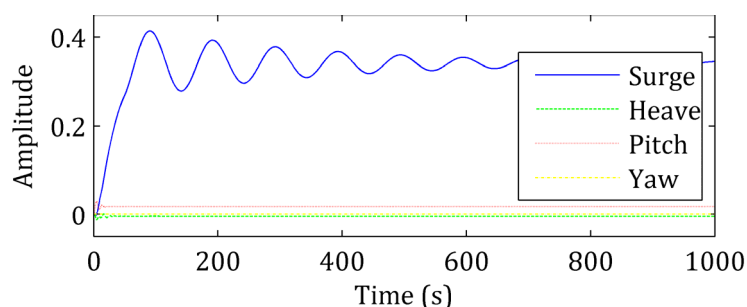


Figure 55. *Ship motion over time in a calm sea. All other DOF are constant. The unit for Surge, Heave and Pitch is metres and the unit for Yaw is degrees.*

Transient in harmonic sea

Simulating the ship motion in a head sea with a significant wave height of 2 m and an incident angle of 180 degrees was tested. The obtained ship response is largely as expected with a harmonic response at the same frequency as the incident wave for, for example, heave and pitch. However, illustrating the response of the surge produces Figure 56 where a long-lasting transient effect may be seen. This response is unphysical and should therefore be reduced.

To limit this effect the ramp length was increased from 50 s to 100s. The ramp length is the length of the period from the start of the simulation during which the incoming wave's amplitude should steadily be increased - here as a smooth function starting at

0 at $t=0$ to the full wave amplitude at the end of this period. Because some improvement is seen, the transient period is further increased to 4 minutes or 240 s, resulting in Figure 57, where a significant improvement in the variations may be seen. Note that in both cases the variations are relatively small after 1,000s. There is, however, still significantly less damping present than would be expected, and further corrections are introduced later.

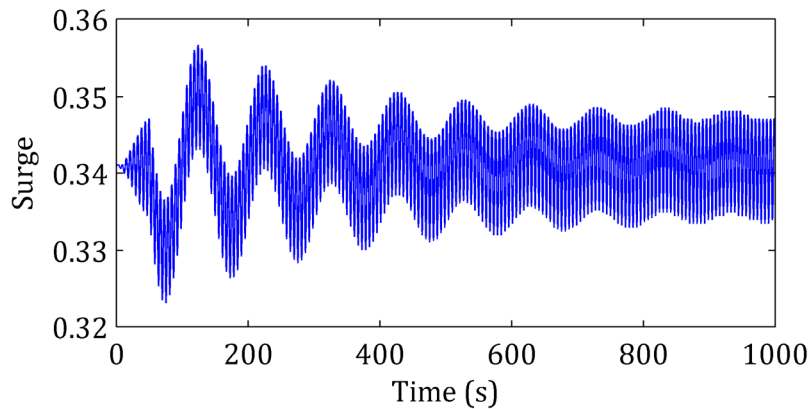


Figure 56. The surge motion of ship in m over time for a ramp length set at 50s.

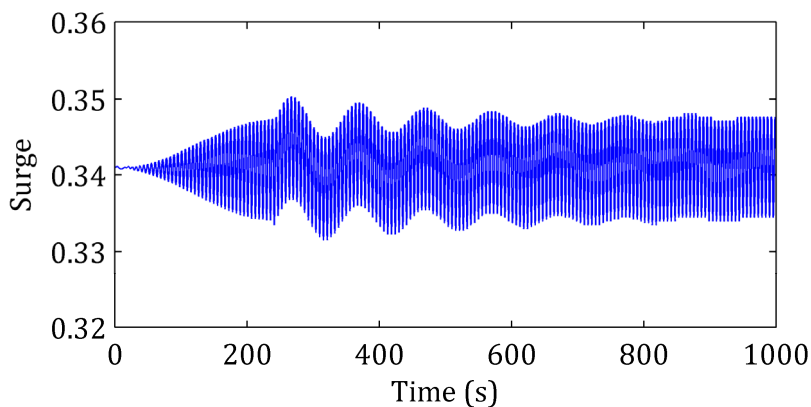


Figure 57. The surge motion of ship in m over time for a ramp length set at 240s.

Numerical solver stability

The software allows for two different methods for numerically solving the differential equation - a first-order and a second-order scheme. It further presents a stability diagram limiting the usability of the two solvers to different cases, giving the stable region as

$$\sqrt{\frac{h_x}{g(\Delta t)^2}} > f(F_h). \quad (40)$$

where f is an increasing monotonic function given as a graph and

$$F_h = \frac{U}{\sqrt{gh_x}}. \quad (41)$$

Here, g denotes the gravitational acceleration, Δt the time step in s, h_x the smallest panel length in the lengthwise direction in metres and U the velocity in m/s. Now, for the used mesh the smallest longitudinal length of any element is found to be $h_x = 5$ m and the greatest velocity of interest is $U = 10$ m/s, giving (for a time step of 0.05s)

$$F_h = \frac{10}{\sqrt{2 \cdot 9.81}} \approx 2.3, \sqrt{\frac{h_x}{g(\Delta t)^2}} \approx 9. \quad (42)$$

By applying the stability diagram in the software manual (DNV, 2011) this indicates that both solvers should be stable for the chosen parameters. However, there is not a wide margin, so the sampling frequency should not be decreased much below 20 Hz due to numerical stability reasons.